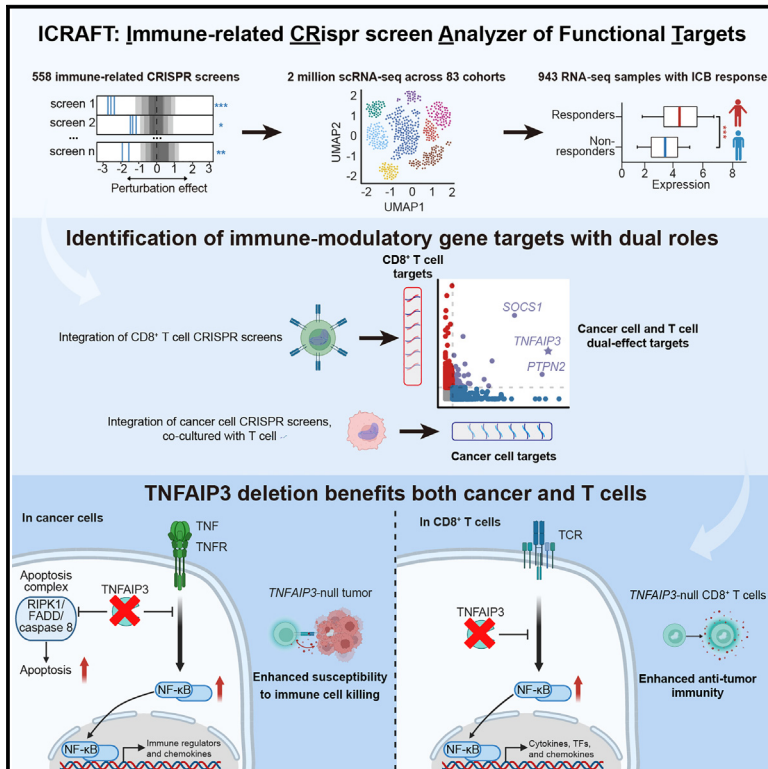# Integrated computational analysis identifies therapeutic targets with dual action in cancer cells and T cells

Graphical abstract

Authors

Ce Luo, Rui Zhang, Rui Guo, ...,
Zhidong Gao, Deng Pan, Zexian Zeng

Correspondence

gaozhidong@pkuph.edu.cn (Z.G.),
dpan@tsinghua.edu.cn (D.P.),
zexianzeng@pku.edu.cn (Z.Z.)

In brief

Existing cancer immunotherapy target discovery platforms typically focus on a single cell type. Luo et al. develop ICRAFT, an interactive platform that integrates CRISPR screens and transcriptomic datasets to identify immunomodulatory gene targets across multiple cell types, providing causal insights into gene perturbations and immune-related phenotypes.

Highlights

- ICRAFT is an interactive platform for identifying immunomodulatory targets

- ICRAFT reveals causal links between gene perturbations and immune phenotypes

- ICRAFT identified key immuno-oncology targets, including TNFAIP3, PTPN2, and SOCS1

- TNFAIP3 deletion enhances immune-mediated cancer cell killing in T and cancer cells

CellPress

Resource

Integrated computational analysis identifies therapeutic targets with dual action in cancer cells and T cells

Ce Luo,[1,16] Rui Zhang,[2,16] Rui Guo,[2,16] Lijian Wu,[3] Teng Xue,[4] Yufeng He,[2] Yiteng Jin,[1] Yanping Zhao,[5] Zongxu Zhang,[1] Peng Zhang,[2] Sitong Ye,[6,7] Xiaohong Li,[2] Dian Li,[8] Wubing Zhang,[9] Chenfei Wang,[10,11] Luhua Lai,[1,2,4] Qiang Pan-Hammarström,[12] Kai W. Wucherpfennig,[13,14] Zhidong Gao,[15,*] Deng Pan,[3,5,*] and Zexian Zeng[1,2,4,17,*]

[1]Center for Quantitative Biology, Academy for Advanced Interdisciplinary Studies, Peking University, Beijing 100084, China
[2]Peking-Tsinghua Center for Life Sciences, Academy for Advanced Interdisciplinary Studies, Peking University, Beijing 100084, China
[3]School of Basic Medical Sciences, Tsinghua University, Beijing 100084, China
[4]Peking University Chengdu Academy for Advanced Interdisciplinary Biotechnologies, Chengdu, Sichuan 610213, China
[5]Tsinghua-Peking Center for Life Sciences, Tsinghua University, Beijing 100084, China
[6]Department of Biomedical Engineering, Yale University, New Haven, CT 06511, USA
[7]Yale School of Medicine, New Haven, CT 06510, USA
[8]Division of Biology and Biomedical Sciences, Washington University in St. Louis School of Medicine, Saint Louis, MO 63108, USA
[9]Institute for Stem Cell Biology and Regenerative Medicine, Stanford University, Stanford, CA 94305, USA
[10]Shanghai Putuo District People's Hospital, School of Life Sciences and Technology, Tongji University, Shanghai 200092, China
[11]Frontier Science Center for Stem Cells, School of Life Sciences and Technology, Tongji University, Shanghai 200092, China
[12]Division of Immunology, Department of Medical Biochemistry and Biophysics, Karolinska Institutet, Stockholm 17165, Sweden
[13]Department of Cancer Immunology and Virology, Dana-Farber Cancer Institute, Boston, MA 02215, USA
[14]Harvard Medical School, Boston, MA 02215, USA
[15]Department of Gastroenterological Surgery, Peking University People's Hospital, Beijing 100084, China
[16]These authors contributed equally
[17]Lead contact
*Correspondence: gaozhidong@pkuph.edu.cn (Z.G.), dpan@tsinghua.edu.cn (D.P.), zexianzeng@pku.edu.cn (Z.Z.)
https://doi.org/10.1016/j.immuni.2025.02.007

SUMMARY

Many cancer drugs that target cancer cell pathways also impair the immune system. We developed a computational target discovery platform to enable examination of both cancer and immune cells so as to identify pathways that restrain tumor progression and potentiate anti-tumor immunity. Immune-related CRISPR screen analyzer of functional targets (ICRAFT) integrates immune-related CRISPR screen datasets, single-cell RNA sequencing (scRNA-seq) data, and pre-treatment RNA-seq data from clinical trials, enabling a systems-level approach to therapeutic target discovery. Using ICRAFT, we identified numerous targets that enhance both cancer cell susceptibility to immune attack and T cell activation, including tumor necrosis factor (TNF) alpha-induced protein 3 (TNFAIP3), protein tyrosine phosphatase non-receptor type 2 (PTPN2), and suppressor of cytokine signaling 1 (SOCS1). In cancer cells, Tnfaip3 (A20) deletion activated the TNF-nuclear factor kappa-B (NF-κB) pathway, promoting chemokine expression and T cell recruitment to the tumor. T cell-mediated elimination of Tnaifp3-null cancer cells was primarily driven by TNF-induced apoptosis. Inactivation of Tnfaip3 in T cells enhanced anti-tumor efficacy. By integrating diverse functional genomics and clinical datasets, ICRAFT provides an interactive resource toward a deeper understanding of anti-tumor immunity and immuno-oncology drug development.

INTRODUCTION

Immune checkpoint blockade (ICB) has remarkable therapeutic effects across different cancer types. The combination of immunotherapy approaches that target different pathways has long-term clinical benefits.[1–4] However, clinical benefits are seen in only a subset of patients, and resistance often emerges among individuals who initially exhibit responses.[5,6] These observations

have steered research in two directions. The first direction seeks to identify biomarkers that predict therapeutic response, including PD-L1 (programmed death ligand 1) expression,[7] microsatellite instability (MSI),[8–10] tumor mutation burden (TMB),[11,12] and genetic profiles derived from next-generation sequencing technology,[13,14] thereby optimizing patient selection for existing treatments. The second direction focuses on new treatment modalities, including chimeric antigen receptor (CAR) T cell
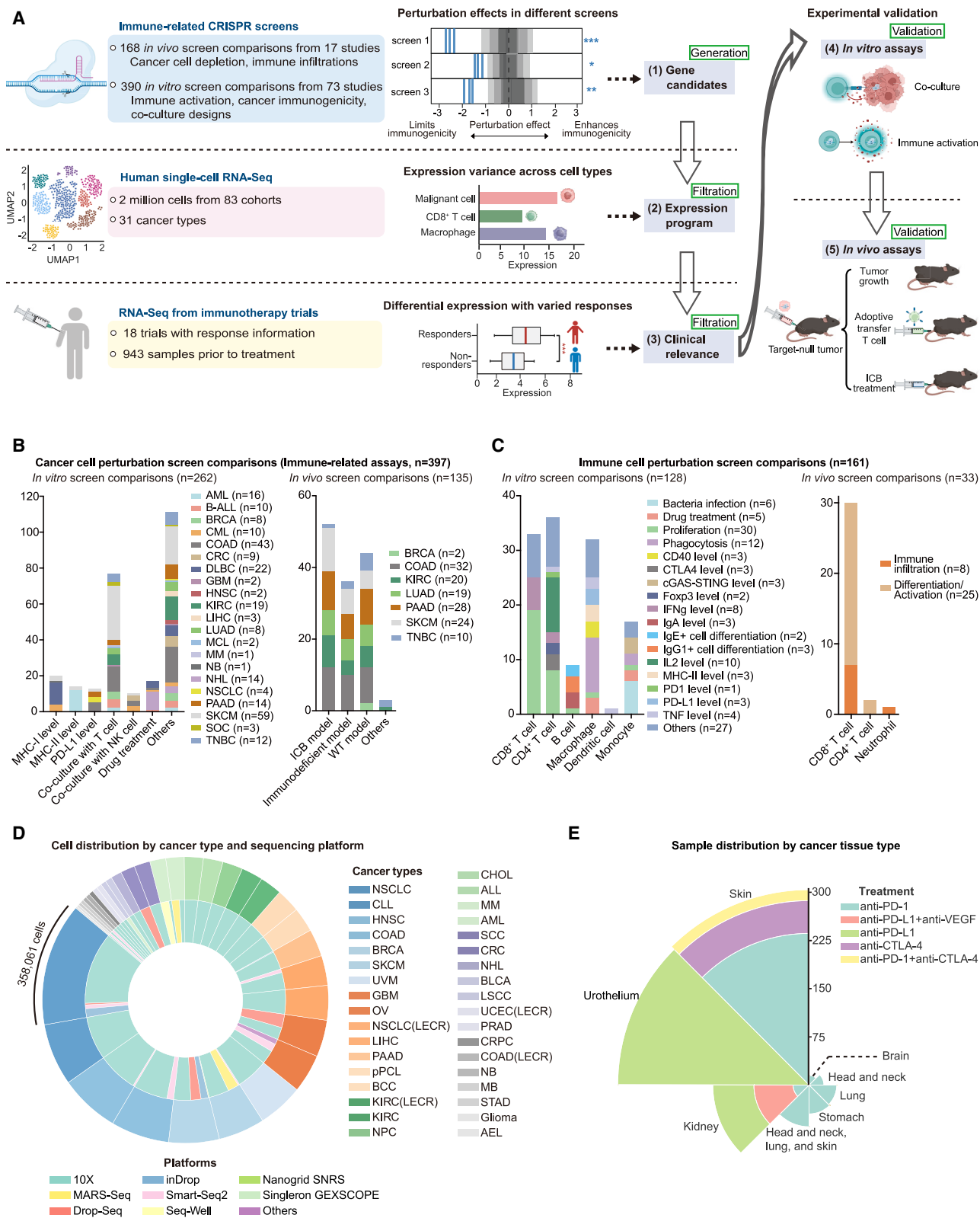
Figure 1. Characterization of ICRAFT

(A) ICRAFT incorporates 168 *in vivo* and 390 *in vitro* immune-related screen comparisons from 90 independent studies, alongside 2 million single-cell gene expression datasets from 83 cohorts and RNA-seq data from 943 patients across 18 ICB trial cohorts.

therapy,[15] T cell receptor-engineered T cells (TCR-T),[16–18] cytokine treatment,[19–22] tumor-infiltrating lymphocyte (TIL) therapy,[23] and the exploration of novel immunotherapy targets.[24–26] Among these strategies, immunotherapy target exploration plays a crucial role. Targeting pathways such as PD-1 (programmed cell death protein 1), CTLA-4 (cytotoxic T-lymphocyte-associated antigen 4), and HER2 (human epidermal growth factor receptor 2) has revolutionized the treatment of various cancers.[4,27,28] Therefore, the pursuit of new targets, especially in the context of tumor immunity, is a promising strategy to improve immunotherapy efficacy.

CRISPR screens are high-throughput genetic approaches to identify genes whose perturbation results in a specific functional outcome.[29,30] This technique is widely applied to identify genetic determinants critical for tumor immune evasion and immune response. Ablation of genes such as *PBRM1*,[31] *GLUT1*,[26] and components in the interferon (IFN)-γ receptor signaling pathway[32] sensitizes cancer cells to T cell-mediated cytotoxicity. Further, loss of function (LOF) of genes including *PTPN2*,[33] *ADAR1*,[34] *COP1*,[35] and *SETDB1*,[36] as revealed by pooled *in vivo* CRISPR screens, enhances the efficacy of immunotherapeutic interventions. CRISPR screens are also useful in investigating phenotypes in immune cells, notably T cells, including aspects such as proliferation,[37] cytokine secretion,[38,39] activation,[40,41] dysfunction,[42,43] and resilience to inhibitory conditions.[44] There is a large body of CRISPR screen datasets, providing causal relationships between gene perturbations and immune-related phenotypes. Integrating these CRISPR-derived datasets with other multi-omics data presents an opportunity to identify robust functional gene targets for enhancing tumor immunity.

Tumor necrosis factor (TNF) alpha-induced protein 3 (TNFAIP3), a ubiquitin-editing enzyme also known as A20, inhibits nuclear factor kappa-B (NF-κB) activation and TNF-induced apoptosis.[45–48] TNFAIP3 also plays roles in IFN signaling,[47,49] promotes autophagy,[50] and inhibits pyroptosis, necroptosis, apoptosis, or a combination of these cell death forms.[51] Polymorphisms in the *TNFAIP3* locus are linked to inflammatory diseases.[52,53] Deleterious mutations in *TNFAIP3* induce early-onset systemic inflammation in patients.[54] Clinically, inactivation of TNFAIP3 in B cell lymphomas is associated with disease pathogenesis,[55–57] whereas *TNFAIP3* mutations are linked to higher survival rates in T cell lymphoma patients.[58] In cancer cells, TNFAIP3 appears to be involved in immune evasion through the suppression of the "eat-me" signal, mediated by the increased expression of *STC1*.[59] Furthermore, deletion of *TNFAIP3* in murine lung adenocarcinoma (LUAD) cells increases susceptibility to anti-PD-L1 therapy.[60] In melanoma cells, TNFAIP3 enhances PD-L1 expression via the STAT3 (signal transducer and activator of transcription 3) signaling pathway.[61] Thus, TNFAIP3 has multifaceted and intricate effects on carcinogenesis and disease progression, making it difficult to distinguish cell-specific roles in the complex tumor microenvironment.

Many cancer treatments designed to target cancer cells inadvertently impair the immune system. Additionally, most gene targets derived from correlative transcriptomic studies lack direct functional effects, making it challenging to establish causal relationships between gene perturbations and immune-related phenotypes. To address these gaps, we developed immune-related CRISPR screen analyzer of functional targets (ICRAFT), an interactive web platform with large-scale curated CRISPR screen data and transcriptomic datasets. ICRAFT enables the systematic identification of immune-modulatory targets with dual effects on both cancer and immune cells. In total, ICRAFT has assembled datasets from 558 immune-related CRISPR screen comparisons from 90 studies, transcriptomic data from over 2 million single cells, and 943 pre-treatment RNA sequencing (RNA-seq) samples from immunotherapy clinical trial participants. Using ICRAFT, we identified several genes, including *TNFAIP3*, *PTPN2*, and *SOCS1*, whose elimination induced beneficial anti-tumor effects by impacting both cancer and T cells. Our findings provide further evidence that *PTPN2* and *SOCS1* perform dual roles in both cancer and T cells.[33,62–67] We found that inactivation of *TNFAIP3* enhanced anti-tumor function. *TNFAIP3* inactivation in cancer cells resulted in a potent T cell-mediated immune response, characterized by increased infiltration of tumors by CD8+ T cells. *TNFAIP3* inactivation in T cells enhanced cytotoxic capability by activating the NF-κB pathway. These findings suggest that targeting *TNFAIP3* can provoke an immune response against tumors by rendering resistant tumors more vulnerable to immune-mediated cytotoxicity and enhancing the anti-tumor capabilities of T cells. Together, these data showcase the effectiveness of ICRAFT in identifying gene targets that have immune-modulatory effects, which will be a valuable resource to the cancer immunology and immunotherapy community.

RESULTS

ICRAFT for immune-modulating gene identification

The evaluation of a gene target for its potential as an immune-therapeutic candidate involves the analysis of several pivotal factors, including the effects of gene perturbation, the cell type where the gene is expressed, and the gene's potential to induce immunotherapeutic responses. To facilitate these analyses, we developed ICRAFT, an interactive web server publicly available at https://icraft.pku-genomics.org/, to streamline the identification of gene targets with immune-modulatory effects (Figure 1A). ICRAFT includes 558 immune-related CRISPR screen comparisons from 90 studies (Table S1), single-cell RNA-seq (scRNA-seq) data from 2 million cells (Table S2), and 943 pre-immunotherapy treatment RNA-seq samples from participants in clinical trials (Table S3). Within the 558 immune-related CRISPR screen comparisons, 397 comparisons were performed on cancer cells, investigating a range of phenotypes such as membrane expression levels of major histocompatibility complex (MHC)-I, MHC-II,

(B) Breakdown of cancer cell perturbation screen comparisons.
(C) Breakdown of immune cell perturbation screen comparisons.
(D) Overview of the 83 scRNA-seq datasets.
(E) Overview of the 943 pre-immunotherapy RNA-seq samples from participants in clinical trials.
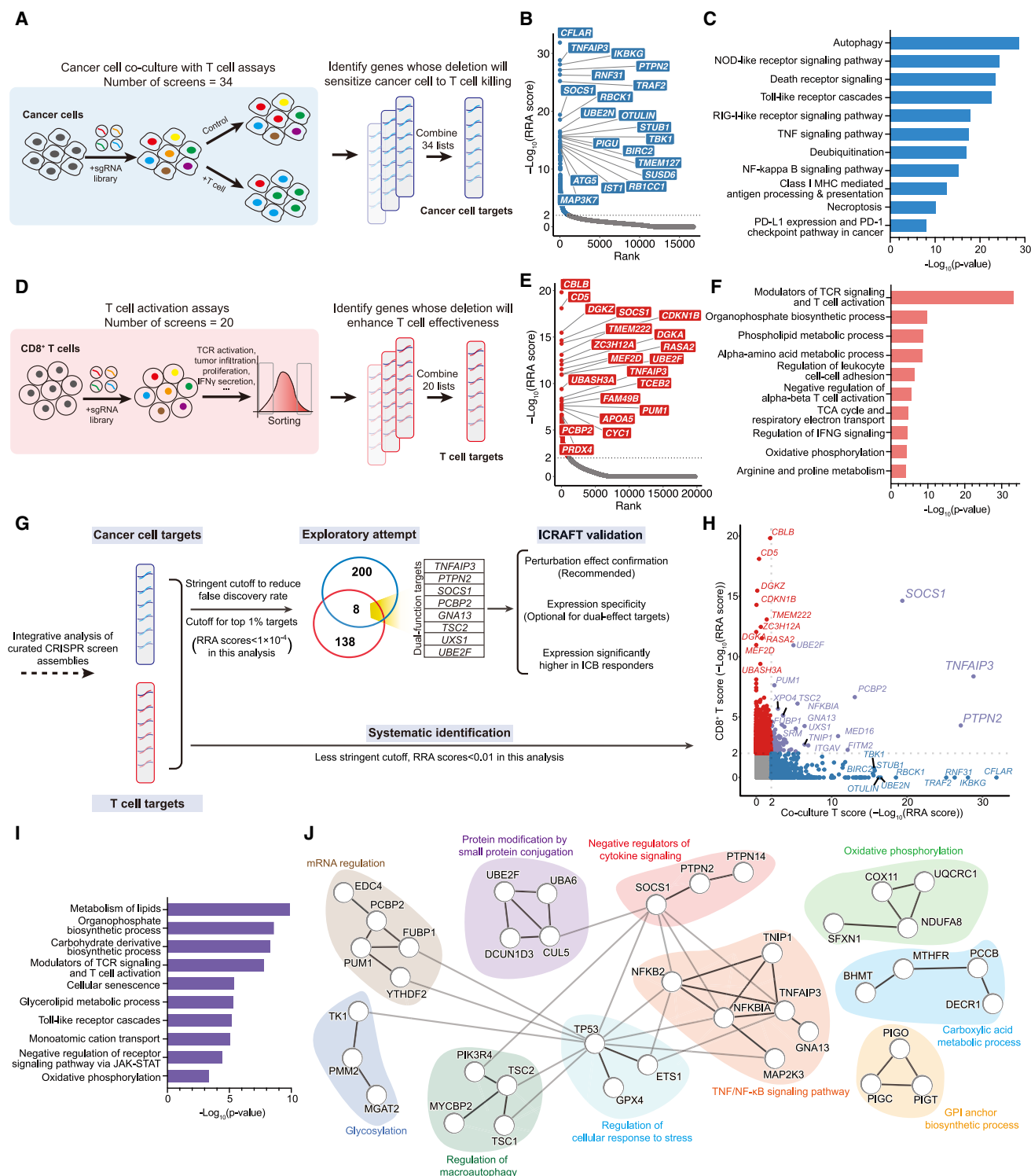See also Figure S1 and Tables S1, S2, and S3.

Figure 2. Integrative analyses of CRISPR screen datasets reveal gene targets with dual roles in cancer and T cells

(A) Illustration of the integrative analyses to identify gene targets in cancer cells to enhance T cell-mediated cytotoxicity.

(B and C) (B) Rank plot showing the top 20 genes, and (C) over-representation enrichment analysis of the top 146 gene targets (RRA scores < 0.0001) derived from (A).

(D) Illustration of the integrative analyses to identify gene targets in T cells to enhance T cell fitness.

(E and F) (E) Rank plot labeling the top 20 genes, and (F) over-representation enrichment analysis of the top 208 gene targets (RRA scores < 0.0001) derived from (D).

and PD-L1, along with the effects of gene perturbation in co-culture assays with CD8$^+$ T cells and natural killer (NK) cells (Figure 1B). 161 CRISPR comparisons focused on immune cells, including CD8$^+$ T, CD4$^+$ T, B cells, macrophages, dendritic cells, and neutrophils. These screens evaluated various phenotypes, including the production of IFN-γ, IL-2, and TNF, as well as cell proliferation, activation, and phagocytosis (Figure 1C). Additionally, among the compiled datasets, 168 comparisons were conducted *in vivo*, examining phenotypes related to immune infiltration and cytotoxicity, cell differentiation, and immune activation (Figures 1B and 1C). Moreover, ICRAFT incorporated 83 scRNA-seq datasets curated from the public domain, encompassing 2 million cells across 31 cancer types (Figure 1D; Table S2; see STAR Methods). To examine clinical relevance, ICRAFT includes data from 943 pre-ICB treatment samples from 18 clinical trial cohorts (Figure 1E; Table S3; see STAR Methods). Together, these data were curated, processed, and quality-controlled through standardized tools and pipelines (see STAR Methods).

ICRAFT streamlines the identification of gene targets that have immunomodulatory effects (Figure 1A). A case in point is the *B2m* gene, the inactivation of which impairs T cell recognition and activation.[68,69] Our analysis through ICRAFT illustrates that the loss of *B2m* in cancer cells compromises T cell-mediated cytotoxicity across various CRISPR screen datasets (Figure S1A), thereby demonstrating ICRAFT's capacity to assess the functional immunomodulatory impact of gene targets. ICRAFT also enables users to evaluate the expression of gene targets of interest across different cell types. For instance, *PDCD1*, which encodes an immune-inhibitory receptor predominately expressed in activated T cells.[70–72] Our analysis of *PDCD1* expression across 23 cell types revealed a significant presence in CD8$^+$ T cells, particularly within their activated subsets (Figure S1B). In our assembled datasets, *PDCD1* expression levels were notably higher in individuals responding to treatment (Figure S1C), aligning with prior studies that link *PDCD1*'s expression to immunotherapeutic efficacy.[73,74]

ICRAFT enables researchers to juxtapose datasets or perform comparative evaluations of their own screening data against ICRAFT datasets. To illustrate, we conducted a comparative analysis of two datasets within ICRAFT, one focusing on T cell response to Treg by co-culture and another on TCR stimulation, both using T cell proliferation as readout.[44] Beyond identifying TCR signaling essential components (*LCP2*, *CD3D*, and *CD247*) and the key negative regulators (*CBLB*[75] and *DGKA*[76]) as positive controls, our analysis further elucidated *RASA2* as a consistently prominent negative regulator of T cell activation (Figure S1D), reinforcing existing research on the critical roles of RASA2 in T cell dysfunction.[44] Moreover, ICRAFT allows comparative analysis of various datasets. Illustratively, we performed a comparative study involving five CRISPR screen datasets, the majority of which were generated to explore primary CD8$^+$ T cells under various immunosuppressive conditions, aiming to identify robust regulators of T cell dysfunction (Figure S1E).

Ablation of *SOCS1*, *PTPN2*, or *TNFAIP3* increases anti-tumor immunity

We leveraged ICRAFT to identify gene targets whose inhibition would robustly and substantially sensitize cancer cells to T cell-mediated cytotoxicity. We performed integrative analyses on the ICRAFT CRISPR screen datasets using the robust rank aggregation (RRA) algorithm[77] (see STAR Methods). These analyzed CRISPR screen datasets were produced under conditions where cancer cells had been transduced with a genome-scale single guide RNA (sgRNA) library and subsequently co-cultured with activated cytotoxic T cells (Figure 2A). A total of 34 genome-scale screen datasets, spanning 18 cell lines across 11 different cancer types, were incorporated for evaluation (Figure S1F; Table S4). Several key regulators of T cell-mediated tumor immunity were identified among the top 20 genes, including genes within the NF-κB (*TRAF2*, *BIRC2*, and *TNFAIP3*), JAK-STAT (*PTPN2* and *SOCS1*), and MHC-I antigen presentation (*TMEM127* and *SUSD6*) pathways, demonstrating that key regulators could be robustly identified (Figures 2B and 2C; Table S5). In addition, we investigated gene targets that confer resistance to cytotoxic T lymphocyte (CTL)-mediated cytotoxicity in cancer cells. The top 20 enriched genes were associated with the IFN-γ signaling (*JAK1*, *STAT1*, *IFNGR1*, and *IFNGR2*) and the MHC-I antigen presentation (*B2M*, *TAP1*, and *TAP2*) pathways (Figures S1G and S1H). Notably, mutations within genes involved in the NF-κB, IFN, and MHC-I pathways have been reported to confer cancer cells resistance to immunotherapeutic interventions.[78,79]

We next utilized ICRAFT to pinpoint gene targets whose inhibition could robustly and substantially improve T cell functionality. CRISPR screen datasets generated to study CD8$^+$ T cells were retrieved from ICRAFT and analyzed (Figure 2D; see STAR Methods). This involved the integration and analysis of 20 CRISPR screen datasets focused on CD8$^+$ T cells. These datasets were originally generated to evaluate phenotypes related to T cell activation, proliferation, tumor infiltration, and IFN-γ secretion (Figure S1I; Table S4). Our integrative analysis identified several positive control genes, including key regulators within TCR signaling (*CBLB*, *CD5*, and *TMEM222*), IFN-γ signaling (*SOCS1*), and TNF-NF-κB signaling (*TNFAIP3*) pathways (Figures 2E and 2F; Table S5). Notably, genes associated with mitochondrial fitness and oxidative phosphorylation (OXPHOS) regulation (*ZC3H12A* and *CYC1*), alongside diacylglycerol kinases (*DGKZ* and *DGKA*), also ranked as top 20 candidates (Figures 2E and 2F; Table S5). This finding is congruent with recent studies highlighting the pivotal roles of mitochondrial metabolism and energy production in the anti-tumor function of CD8$^+$ T cells.[80–82] Furthermore, we extended the analyses to identify gene targets whose inactivation induces T cell dysfunction and revealed significant involvement of TCR signaling (*LCP2*, *VAV1*, *CD247*, and *ZAP70*) and tRNA metabolism (*AARS*, *FARSA*) pathways (Figures S1J and S1K).

(G and H) Flow diagram of the target discovery process (G), highlighting gene targets common to both analyses in cancer and T cells. Scatter plot of the systematic target identification result (H). Statistical cutoffs for RRA scores are 0.0001 in (G) and 0.01 in (H).

(I and J) Over-representation enrichment analysis (I) and PPI network analysis (J) to examine the 82 targets identified with dual roles in both cancer and T cells in (H).

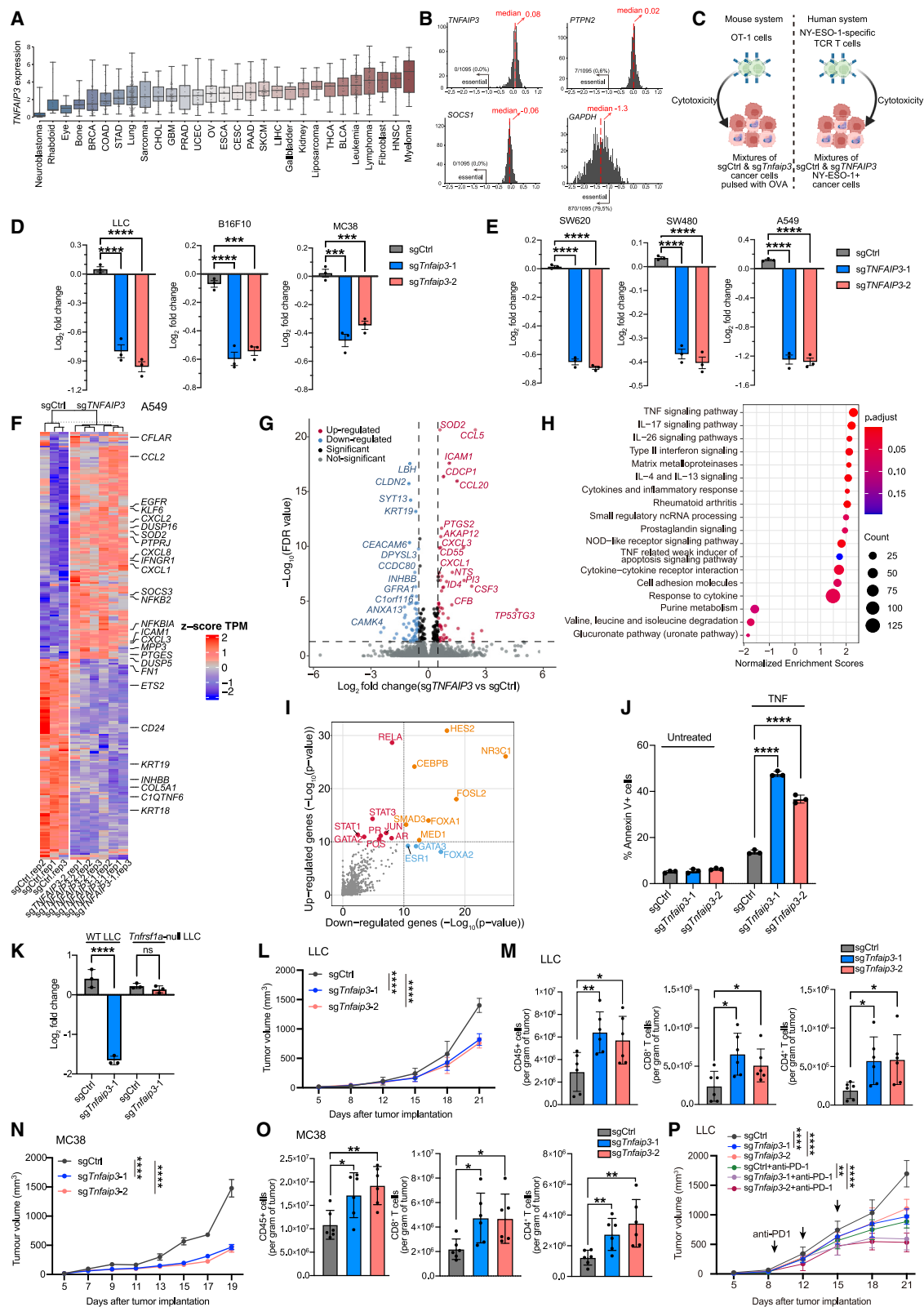See also Figure S1 and Tables S4 and S5.

Figure 3. *TNFAIP3* deletion in cancer cells enhances their sensitivity to CD8+ T cell-mediated cytotoxicity

(A) *TNFAIP3* mRNA levels across 1,208 cancer cell lines from the CCLE.

(B) Evaluation of *TNFAIP3*, *PTPN2*, *SOCS1*, and negative control *GAPDH*'s gene essentiality using CRISPR screen data of 1,095 cell lines from the DepMap portal. A negative score indicates high essentiality, and the red line indicates the median score.

(legend continued on next page)

In the aforementioned analyses, we obtained gene targets whose suppression enhances the sensitivity of cancer cells to T cell-mediated cytotoxicity and gene targets whose inactivation could enhance T cell functions. An exploratory analysis using a stringent cutoff (RRA score < 0.0001) identified eight overlapping gene targets between the two analyses (Figure 2G), highlighting a subset of genes that play a critical role in both cancer cells and CD8+ T cells within the tumor immune microenvironment. Next, we performed a systematic analysis with a less stringent cutoff (RRA score < 0.01), which expanded the list to 82 genes, with *SOCS1*, *PTPN2*, and *TNFAIP3* as the leading ones (Figure 2H; Table S5). Recent studies have highlighted the dual roles of suppressor of cytokine signaling 1 (SOCS1) and protein tyrosine phosphatase non-receptor type 2 (PTPN2) in both cancer and immune cells.[33,62–67] SOCS1 inactivation leads to increased cytokine-induced apoptosis in cancer cells[66] and enhanced proliferation and activation of CD8+ T cells.[67] Similarly, PTPN2 loss in cancer cells improves their sensitivity to IFN-γ and their response to ICB,[33] while its inactivation boosts CD8+ T cell anti-tumor activity by modulating JAK-STAT signaling.[62–64] A novel inhibitor targeting PTPN2-PTPN1 was recently developed, sensitizing cancer cells to IFN-γ and at the same time activating immune cells, thus inducing potent anti-tumor immunity in ICB-resistant mouse models.[65] Pathway enrichment analysis of the 82 dual-effect genes highlighted several pathways, including TCR signaling and T cell activation, Toll-like receptor cascades, JAK-STAT signaling pathway, and lipid OXPHOS metabolism (Figure 2I). Subsequent protein-protein interaction (PPI) network analysis elucidated that these dual-effect targets are predominantly enriched in the TNF-NF-κB signaling pathway, glycosylation process, regulation of macroautophagy, carboxylic acid metabolic process, and glycosylphosphatidylinositol (GPI) anchor biosynthesis (Figure 2J).

Inactivation of *TNFAIP3* in cancer cells sensitizes them to CD8+ T cell-mediated cytotoxicity

Dual-effect analysis identified *TNFAIP3* as a key target alongside *SOCS1* and *PTPN2*. The dual functions of SOCS1 and PTPN2 in both cancer and CD8+ T cells are well recognized.[33,62–65] Analysis of RNA-seq and proteomics data from 1,208 human cancer cell lines in the Cancer Cell Line Encyclopedia (CCLE)[83] uncovered high-level yet variable TNFAIP3 expression patterns (Figures 3A and S2A). Correlation analysis of proteomics data from the CCLE datasets identified key pathways associated with TNFAIP3 abundance, including antigen processing (TAP1, TAP2, and TAPBP), cellular response to IFN-γ (IFI16), and phagosome (CTSL) (Figures S2B and S2C). Conversely, negatively correlated proteins were linked to ATP-dependent chromatin remodeling (MBD3 and BRD7) and the polycomb repressive complex (PCGF2) (Figures S2B and S2C).

Further analysis of 1,095 human cancer cell lines from the Cancer Dependency Map (DepMap) project[83] indicated that *in vitro* proliferation and viability of cancer cells remained unaffected by the inactivation of *TNFAIP3*, alongside *SOCS1* and *PTPN2* (Figure 3B). We next investigated whether TNFAIP3 deficiency sensitized cancer cells to CTL-mediated killing. We generated *TNFAIP3*-null murine and human cancer cell lines by CRISPR-mediated mutagenesis and performed *in vitro* competition assay by co-culturing edited cancer cells with cytotoxic T cells (Figure 3C). The genetic deletion efficiency was confirmed by western blot analysis (Figure S2D). Notably, the inactivation of *Tnfaip3* sensitized cancer cells to T cell-mediated killing in LLC, B16F10, and MC38 murine cell lines (Figures 3D and S2E). Similar results were observed in human cancer cell lines (SW620, SW480, and A549) carrying the NY-ESO-1 antigen and co-cultured with the NY-ESO-1 antigen-specific primary CD8+ T cells (Figures 3E and S2F).

RNA-seq analysis demonstrated substantial transcriptomic alterations between *TNFAIP3*-null and control-edited A549 cancer cells (Figure 3F). Notably, *TNFAIP3*-null cells exhibited enhanced expression of NF-κB pathway genes (*NFKBIA* and *NFKB2*), chemokines (*CCL5* and *CCL20*), and immune-signaling molecules (*IFNGR1* and *ICAM1*) relative to control-edited cancer cells (Figures 3F and 3G; Table S6). Gene set enrichment analysis (GSEA) further highlighted transcription activation of various immune-related pathways, including TNF signaling, type 2 IFN signaling, cytokine and inflammatory response, and IL-17 signaling in *TNFAIP3*-null cells (Figure 3H). Additionally, pathways

---

(C) Illustration of *in vitro* competition assay to co-culture sgCtrl and sg*TNFAIP3* cancer cells with antigen-specific CD8+ T cells. The left panel shows the sgCtrl and sg*Tnfaip3* murine cancer cell mixtures were pulsed with OVA peptide (257–264 aa, SIINFEKL) and then co-cultured with pre-activated OT-I T cells. The right panel shows the NY-ESO-1+ sgCtrl and sg*TNFAIP3* human cancer cell mixtures were exposed to activated human CD8+ T cells transduced with NY-ESO-1-specific TCR.

(D and E) Log$_2$ fold change of the percentage of sg*TNFAIP3* cells following co-culture with CD8+ T cells, usingcarboxyfluorescein succinimidyl ester (CFSE) or CellTrace Violet (CTV)-labeled sgCtrl murine (D) and human (E) cancer cells as control. (n = 3 per group.)

(F) RNA-seq analysis of differentially expressed genes between sgCtrl and sg*TNFAIP3* A549 cancer cells (n = 3 per group).

(G) Volcano plot of differentially expressed genes between sg*TNFAIP3* and sgCtrl A549 cancer cells. Statistical significance ($-\log_{10}$ false discovery rate [FDR]) was plotted against $\log_2$ fold change of gene expression levels (sg*TNFAIP3*/sgCtrl cells). The cutoffs are FDR $\leq$ 0.05 and |$\log_2$ fold change| > 0.5

(H) GSEA of pathways upregulated or downregulated in sg*TNFAIP3* versus sgCtrl A549 cancer cells. (NES, normalized enrichment score.)

(I) LISA transcription factor inference based on differentially expressed genes in sg*TNFAIP3* cells, utilizing ChIP-seq data from CistromeDB.

(J) Flow cytometry analysis of annexin V/7AAD staining in sg*Tnfaip3* and sgCtrl LLC cells treated with TNF (10 ng/mL) for 24 h, quantifying annexin V positive cells.

(K) Summary of $\log_2$ fold change in the ratio of sgCtrl to sg*Tnfaip3* LLC cells co-cultured with OT-I T cells (E:T ratio = 1:5), comparing *Tnfrsf1a* ablation to wild-type background.

(L–O) Tumor growth curves for sgCtrl and sg*Tnfaip3* LLC (L) and MC38 (N) tumors in wild-type C57BL/6 mice. (n = 6 per group.) Flow cytometry analysis of immune cell infiltrations in sgCtrl and sg*Tnfaip3* LLC (M) and MC38 (O) tumors.

(P) Tumor growth response of sg*Tnfaip3* or sgCtrl LLC tumors to anti-PD-1 (200 μg/mice) or isotype antibodies (n = 6 per group). Treatments start on day 9 post-tumor inoculation and are administered every 3 days for a total of three times.

Data are represented as mean ± SD (J, K, M, and O) and mean ± SEM (D, E, L, N, and P). *$p < 0.05$, **$p < 0.01$, ***$p < 0.001$, and ****$p < 0.0001$ by two-way ANOVA (J–L, N, and P), one-way ANOVA (D and E), and unpaired Student's t test (M and O). ns, not significant. Data are representative of at least two independent experiments (D, E, J, K, and L–P). See also Figure S2 and Table S6.
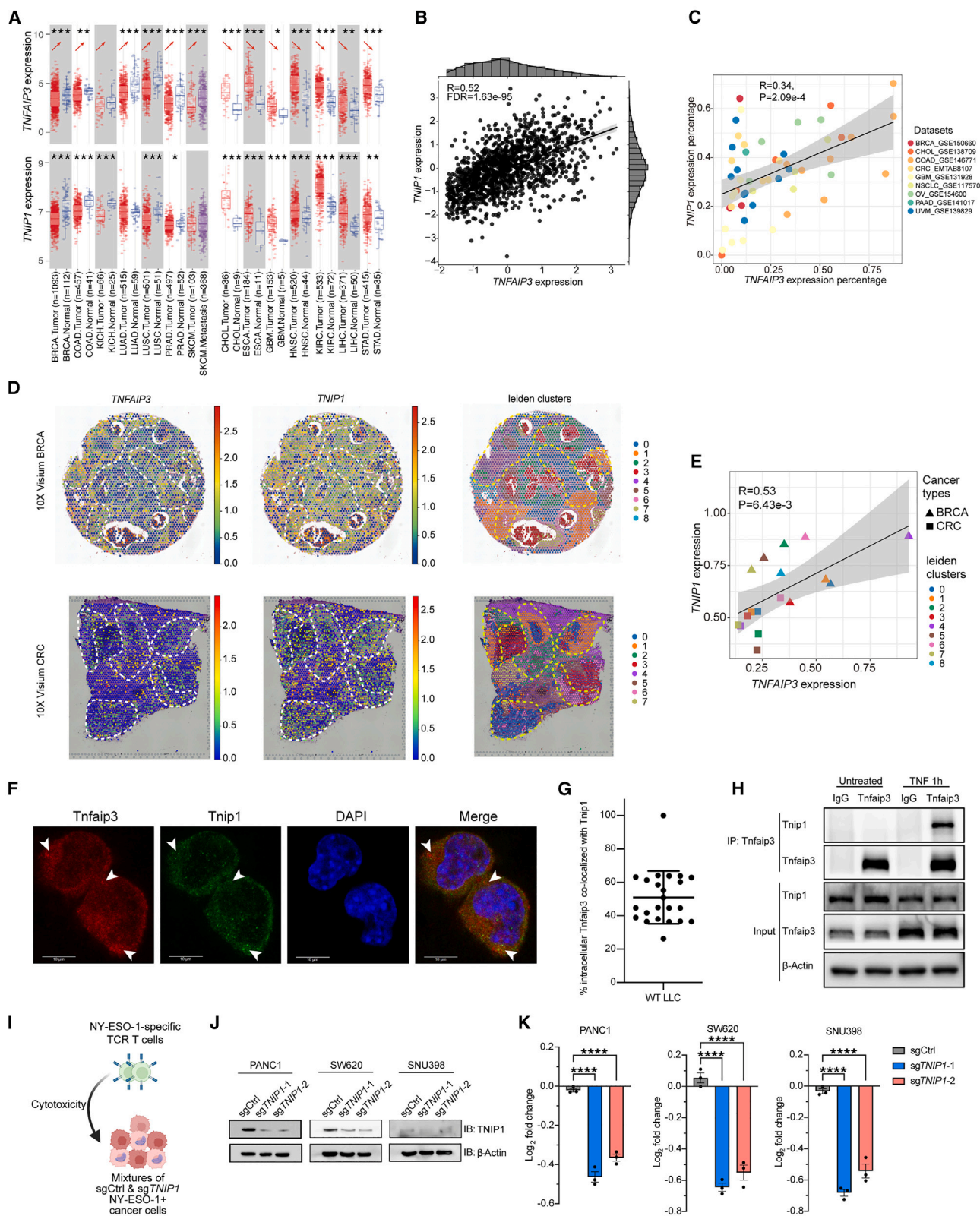
Figure 4. Targeting the TNFAIP3-TNIP1 complex in cancer cells enhances anti-tumor immunity

(A) Comparison of *TNFAIP3* and *TNIP1* expression between tumor tissues and adjacent normal tissues across all TCGA cancer types, showing similar distribution patterns for *TNFAIP3* and *TNIP1* levels.

(legend continued on next page)

related to cell-cell interactions, matrix metalloproteinases, and cell adhesion were activated after *TNFAIP3* deletion (Figure 3H). To infer the transcription factors (TFs) mediating these observed differential gene expressions upon *TNFAIP3* deletion, we applied LISA to identify regulatory TFs through chromatin immunoprecipitation sequencing (ChIP-seq) data and DNA-binding motifs.[84] The LISA analyses implicated the RELA, HES2, NR3C1, CEBPB, STAT, FOX, and AP-1 families of TFs as putative regulators (Figure 3I). Previous studies demonstrated that RELA, AP-1, and CEBPB are important in mediating the expression of immune-signaling molecules in response to TNF stimulation.[85,86] Motif enrichment analysis further reinforced the roles of the FOX and AP-1 families (Figures S2G and S2H). These findings collectively imply that TNF-induced NF-κB pathway activation orchestrates the immune response following *TNFAIP3* inactivation in cancer cells.[87]

In the RNA-seq analysis, the TNF-induced NF-κB pathway was activated after *TNFAIP3* deletion (Figures 3F–3H), implying that the enhanced CTL-mediated cytotoxicity following *TNFAIP3* deletion was mediated by TNF. This hypothesis was tested by treating LLC cells with TNF, with IFN-γ as a comparative control. Notably, *Tnfaip3*-null cells were depleted upon treatment with TNF (Figures 3J and S2I). Further analysis of the recruitment of the apoptotic signaling complex in TNF-treated LLC cells, via co-immunoprecipitation (coIP) using an anti-RIPK1 antibody, revealed an increased presence of caspase-8 and Fas-associated protein with death domain (FADD) in the apoptotic complex of *Tnfaip3*-null cells (Figure S2J). Analysis of IFN-γ-treated groups showed no differential phosphorylation of STAT1 at tyrosine 701 between *Tnfaip3*-null and control-edited cancer cells (Figure S2K). To further validate that TNF is required for sensitizing *Tnfaip3*-null cancer cells to CTL-mediated cytotoxicity, *Tnfaip3* deletion was introduced into TNF receptor-null (*Tnfrsf1a*-null) LLC cells. Co-culture experiments with CD8+ T cells showed that the ablation of the TNF receptor abolished the enhanced susceptibility to cytotoxicity observed in *Tnfaip3*-null cancer cells (Figure 3K), thereby reinforcing that the increased CTL-mediated cytotoxicity observed following *Tnfaip3* deletion is primarily attributed to TNF-induced apoptosis.

To investigate Tnfaip3 in regulating tumor growth under immune selection pressure *in vivo*, we inoculated *Tnfaip3*-null and control-edited LLC cells into wild-type (WT) B6 mice (Figure S2L). Tumors derived from *Tnfaip3*-null cells exhibited a reduced growth rate compared with control-edited cells (Fig-

ure 3L). Examination of TILs revealed a substantial increase in immune cell infiltration within *Tnfaip3*-null tumors, including higher levels of total CD45+ immune cells, CD8+ T cells, and CD4+ T cells (Figure 3M). This experiment was replicated using the MC38 colon cancer model, where *Tnfaip3* inactivation similarly led to delayed tumor progression and increased TILs in the TME (Figures 3N and 3O). Together, these data indicate that Tnfaip3 ablation promotes enhanced immune surveillance *in vivo*. The effect of *Tnfaip3* deletion on tumor responsiveness to ICB therapy was further evaluated. Specifically, control-edited or *Tnfaip3*-null LLC cells were transplanted into the WT B6 mice, which were then treated with either isotype control or anti-PD-1 antibodies (Figure S2M). Remarkably, *Tnfaip3* ablation alone inhibited tumor growth to an extent similar to ICB treatment in *Tnfaip3* WT tumors (Figure 3P). In addition, *Tnfaip3*-null tumors showed a more favorable response to anti-PD-1 therapy compared with control-edited tumors (Figure 3P).

Ablation of TNIP1 in theTNFAIP3-TNIP1 complex facilitates T cell-mediated immunosurveillance

In the integrative analysis, TNFAIP3 interacting protein 1 (*TNIP1*) was also delineated as a leading target that has dual roles in both cancer and T cells (Figures 2H and 2J). TNIP1 interacts with TNFAIP3 via polyubiquitin chains in immune and cancer cells.[88–92] Notably, analysis of The Cancer Genome Atlas (TCGA) datasets[93] revealed that *TNIP1*'s expression patterns closely mirror those of *TNFAIP3* in various cancer types (Figure 4A). Additionally, a robust correlation between *TNIP1* and *TNFAIP3* expressions was observed across the 1,208 human cancer cell lines in CCLE[83] (Figure 4B). Analysis of nine scRNA-seq datasets of 117,256 cancer cells further revealed a significant positive correlation in the expression ratios of *TNIP1* and *TNFAIP3* (Figure 4C). Spatial transcriptomics data from two distinct cancer types demonstrated that expressions of *TNIP1* and *TNFAIP3* are colocalized within specific spatial regions (Figure 4D) and exhibit significant positive correlation across different spatial cellular clusters (Figure 4E).

Confocal microscopy assay confirmed the intracellular colocalization between Tnip1 and Tnfaip3 (Figures 4F and 4G). Moreover, coIP assay confirmed their interaction, which was enhanced following TNF treatment (Figure 4H). Multiple *TNIP1*-null human cancer cell lines (PANC1, SW620, and SNU398) with NY-ESO-1 expression were generated. Subsequently, these cell lines were subjected to a competition assay involving co-culture with NY-ESO-1 antigen-specific primary CD8+ T cells

(B) Correlation between *TNFAIP3* and *TNIP1* expression levels in CCLE datasets.

(C) Correlation between the expression percentages of *TNFAIP3* and *TNIP1* in cancer cells across 9 ICRAFT scRNA-seq datasets.

(D) Spatial feature plots showing *TNFAIP3* and *TNIP1* expression in tissue sections from human breast and colorectal cancer samples, profiled by Visium spatial transcriptomics sequencing.

(E) Spatial correlation between *TNFAIP3* and *TNIP1* transcriptomic expression across different cellular clusters.

(F) Representative confocal microscopy images demonstrating intracellular colocalization of Tnfaip3 with Tnip1 in LLC cells. Scale bars represent 10 μm.

(G) Quantifications of the colocalization between intracellular Tnfaip3 and Tnip1 in LLC cells.

(H) Western blotting analysis following Tnip1 coIP in LLC cells, untreated or treated with TNF (10 ng/mL) for 1 h.

(I) *In vitro* sgCtrl and sg*TNIP1* cancer cell co-culture with primary CD8+ T cell competition assay. The NY-ESO-1+ human cancer cell mixtures were exposed to activated CD8+ T cells expressing the TCR specific for the NY-ESO-1 antigen.

(J) Western blot analysis confirming the genetic deletion efficiency of TNIP1 in different human cell lines.

(K) Log₂ fold change of the percentage of *TNIP1*-null cells following co-culture with CD8+ T cells specific for the NY-ESO-1 antigen.

Data are represented as mean ± SEM (K). *$p < 0.05$, **$p < 0.01$, ***$p < 0.001$, and ****$p < 0.0001$ by Wilcoxon test (A) and one-way ANOVA (K). ns, not significant. Statistical tests performed in (B), (C), and (E) are linear regression analyses. Data are representative of at least two independent experiments (K).
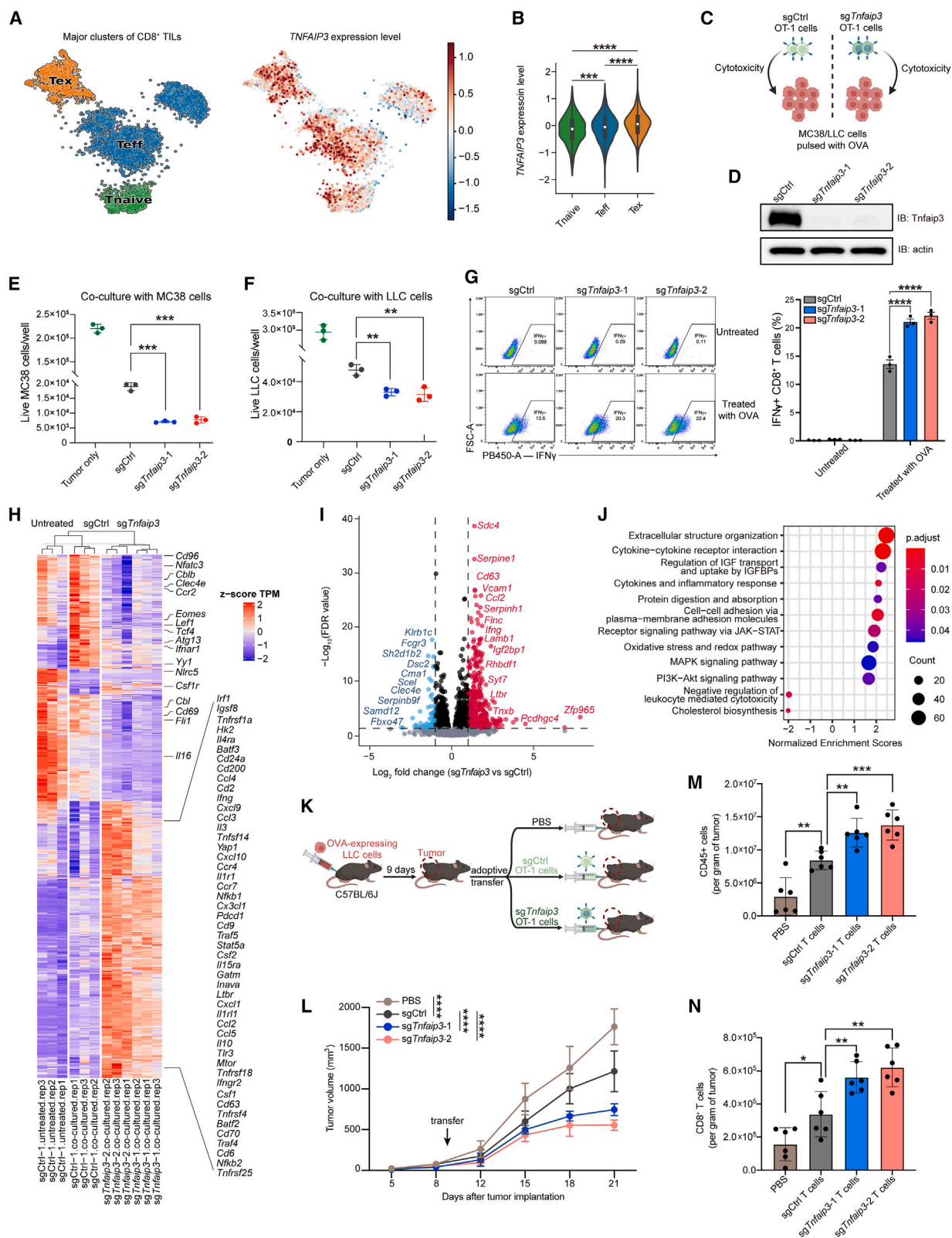
Figure 5. *Tnfaip3* ablation in CD8+ T cells enhances T cell activation and anti-tumor responses

(A) Uniform manifold approximation and projection (UMAP) visualization of major clusters of tumor-infiltrating CD8+ T cells and *TNFAIP3* expression. Tex, exhausted T cells; Teff, effector T cells; Tnaive, naive T cells.

(Figure 4I). The efficiency of *TNIP1* ablation in different cell lines was confirmed by western blot analysis (Figure 4J). Co-culturing *TNIP1*-null cancer cells with NY-ESO-1 antigen-specific T cells demonstrated that *TNIP1* inactivation sensitized cancer cells to T cell-mediated cytotoxicity (Figure 4K), similar to the results observed with *TNFAIP3* deletion (Figure 3E). Therefore, disruption of the TNFAIP3-TNIP1 complex reduces the immune evasion capabilities of cancer cells.

Ablation of *Tnfaip3* in T cells enhances T cell cytotoxicity

Our analysis highlights the dual functions of TNFAIP3 in both cancer and T cells (Figures 2G and 2H), prompting a detailed exploration of its anti-tumor functions in T cells. Data from the Human Protein Atlas[94] indicates that *TNFAIP3* expression is higher in activated T cells than in naive T cells (Figure S3A). This observation was further confirmed by examining the human pan-cancer CD8^{+} TILs[95] (Figures S3B and S3C), where *TNFAIP3* expression levels were higher in exhausted and effector T cells relative to naive T cells (Figures 5A and 5B). We also investigated the gene programs associated with *TNFAIP3* expression across T cell subpopulations. In naive T cells, *TNFAIP3* was positively correlated with genes involved in the TCR signaling pathway (*MALT1*, *NR4A2*, and *NR4A3*) (Figures S3D and S3E). In effector T cells, expression of *TNFAIP3* showed positive correlations with genes in the cytokine-cytokine receptor interaction pathway (*CXCR4*, *CXCR3*, and *TNFRSF9*) and negative correlations with genes in the integrin-mediated signaling pathway (*ITGB2* and *PLEK*) (Figures S3F and S3G). Interestingly, exhausted T cells displayed a positive enrichment in pathways associated with cellular stress response, including cellular senescence (*ZFP36* and *ZFP36L2*) and autophagy (*ATG2A*), alongside a negative enrichment in nucleotide metabolism (*AK5* and *UPP1*) (Figures S3H and S3I).

To investigate the role of TNFAIP3 in modulating the anti-tumor efficacy of CD8^{+} T cells, we engineered *Tnfaip3*-null and control-edited OT-I T cells using retroviral gene editing (see STAR Methods). These engineered OT-I T cells were then co-cultured with MC38 or LLC cancer cells pulsed with ovalbumin (OVA) peptide (257–264 aa, SIINFEKL) for 24 h to assess their cytotoxicity (Figure 5C). The genetic ablation effi-ciency was confirmed by western blot 7 days following editing (Figure 5D). Cytotoxicity assay demonstrated that *Tnfaip3*-null T cells exhibited higher cytotoxicity against MC38 and LLC cancer cells compared with control-edited T cells (Figures 5E and 5F). Furthermore, upon stimulation with the OVA peptide (257–264 aa, SIINFEKL), *Tnfaip3*-null T cells showed a remarkable increase in the expression levels of IFN-γ, an important cytotoxicity marker, relative to control-edited T cells (Figure 5G).

To delineate the effects of *Tnfaip3* deletion on CD8^{+} T cells, we performed RNA-seq on untreated OT-I T cells and those subjected to *Tnfaip3* ablation or intergenic-targeting control ablation, following co-culture with LLC cancer cells. Notably, control-edited T cells stimulated by cancer cells showed an expected increase in *Tnfaip3* expression in response to antigen exposure (Figure S3J). Differential expression analysis revealed a remarkable upregulation of genes associated with the NF-κB pathway (*Nfkb1* and *Nfkb2*), co-stimulatory molecules (*Tnfrsf4* and *Tnfrsf14*), memory program (*Batf3*), and effector molecules involved in the JAK-STAT signaling pathway (*Ifng*) in *Tnfaip3*-null relative to control-edited OT-I T cells (Figures 5H–5J; Table S6). Additionally, there was an upregulation of TNF signaling genes (*Vcam1* and *Tnfrsf1a*), chemokines and chemokine receptors (*Ccl2*, *Ccl3*, *Ccl4*, *Ccl5*, *Ccr4*, *Cxcl1*, *Cxcl9*, *Cxcl10*, and *Cx3cl1*), immune-signaling molecules (*Ltbr*, *Cd24a*, *Cd9*, and *Cd6*), and multiple key TFs (*Irf1* and *Stat5a*) (Figures 5H–5J; Table S6). Remarkably, genes functioning as negative regulators of TCR signaling (*Cbl* and *Cblb*) and modulators of T cell effector differentiation (*Fli1* and *Cd69*) were down-regulated (Figures 5H–5J; Table S6). Utilizing LISA[84] to infer potential TFs underlying the differential gene expression observed upon *Tnfaip3* ablation in OT-I T cells, we identified STAT5A, JUN, and PRC2 components (EZH2, EZH1, EED, and SUZ12) as potential regulators (Figure S3K). Motif enrichment analysis further highlighted JUNB, NFKB2, and BCL6 as putative regulators (Figures S3L and S3M). The PRC2 complex plays a role in mediating chromatin repression, guiding the terminal differentiation of effector CD8^{+} T cells.[96] Collectively, these findings suggest that *Tnfaip3* inactivation enhances effector programming in CD8^{+} T cells.

(B) Violin plot of *TNFAIP3* expression across major CD8^{+} T cell clusters.

(C) *In vitro* co-culture assay setup of sgCtrl and sg*Tnfaip3* edited activated OT-I CD8^{+} T cells co-cultured with either MC38 or LLC cells. CD8^{+} T cells transduced with either sgCtrl or sg*Tnfaip3* sgRNAs were co-cultured with OVA peptide (257–264 aa, SIINFEKL)-pulsed MC38 (E) or LLC (F) cancer cells at E:T ratio of 1:3 (MC38) or 1:6 (LLC). After 24 h, live cancer cells were counted via flow cytometry.

(D) Western blotting showing Tnfaip3 ablation levels in OT-I CD8^{+} T cells.

(E and F) Live MC38 (E) and LLC (F) cancer cell numbers after co-culturing with sg*Tnfaip3* or sgCtrl OT-I CD8^{+} T cells. (*n* = 3 per group).

(G) Flow cytometry quantification of the effector marker IFN-γ in CD8^{+} T cells after OVA peptide (257–264 aa, SIINFEKL) stimulation for 4 h. Representative flow cytometry data (left) and summary bar plots (right) showing the proportion of IFN-γ+ OT-I cells.

(H) RNA-seq analysis of differentially expressed genes in sgCtrl and sg*Tnfaip3* OT-I CD8^{+} T cells co-cultured with OVA peptide (257–264 aa, SIINFEKL)-pulsed LLC cancer cells for 4 h (*n* = 3 per group).

(I) Volcano plot of differentially expressed genes between sg*Tnfaip3* and sgCtrl OT-I cells. Statistical significance ($-\log_{10}$ FDR) was plotted against $\log_2$ fold change in gene expression. The cutoffs used in the analysis are FDR $\leq$ 0.05 and |$\log_2$ fold change| > 0.5

(J) GSEA showing pathways upregulated and downregulated in sg*Tnfaip3* versus sgCtrl OT-I cells. (NES, normalized enrichment score).

(K) Overview of the adoptive T cell transfer experiment design *in vivo*. LLC-OVA cancer cells (1 × 10^{6}) were implanted subcutaneously, and edited OT-I CD8^{+} T cells (3 × 10^{6}) were transferred via tail vein injection on day 9 post-inoculation.

(L) Tumor growth curves for adoptively transferred sg*Tnfaip3*-1, sg*Tnfaip3*-2, or sgCtrl OT-I CD8^{+} T cells. (*n* = 6 per group).

(M and N) Flow cytometry analysis of infiltrated total immune cells (CD45^{+}) (M) and CD8^{+} T cells (N) within LLC tumors after adoptive transfer of sgCtrl or sg*Tnfaip3* OT-I CD8^{+} T cells.

Data are represented as mean ± SD (E–G and L–N). *p < 0.05, **p < 0.01, ***p < 0.001, and ****p < 0.0001 by Wilcoxon test (B), unpaired Student's t test (E, F, M, and N), and two-way ANOVA (G and L). Data are representative of at least two independent experiments (E–G and L–N). See also Figure S3 and Table S6.

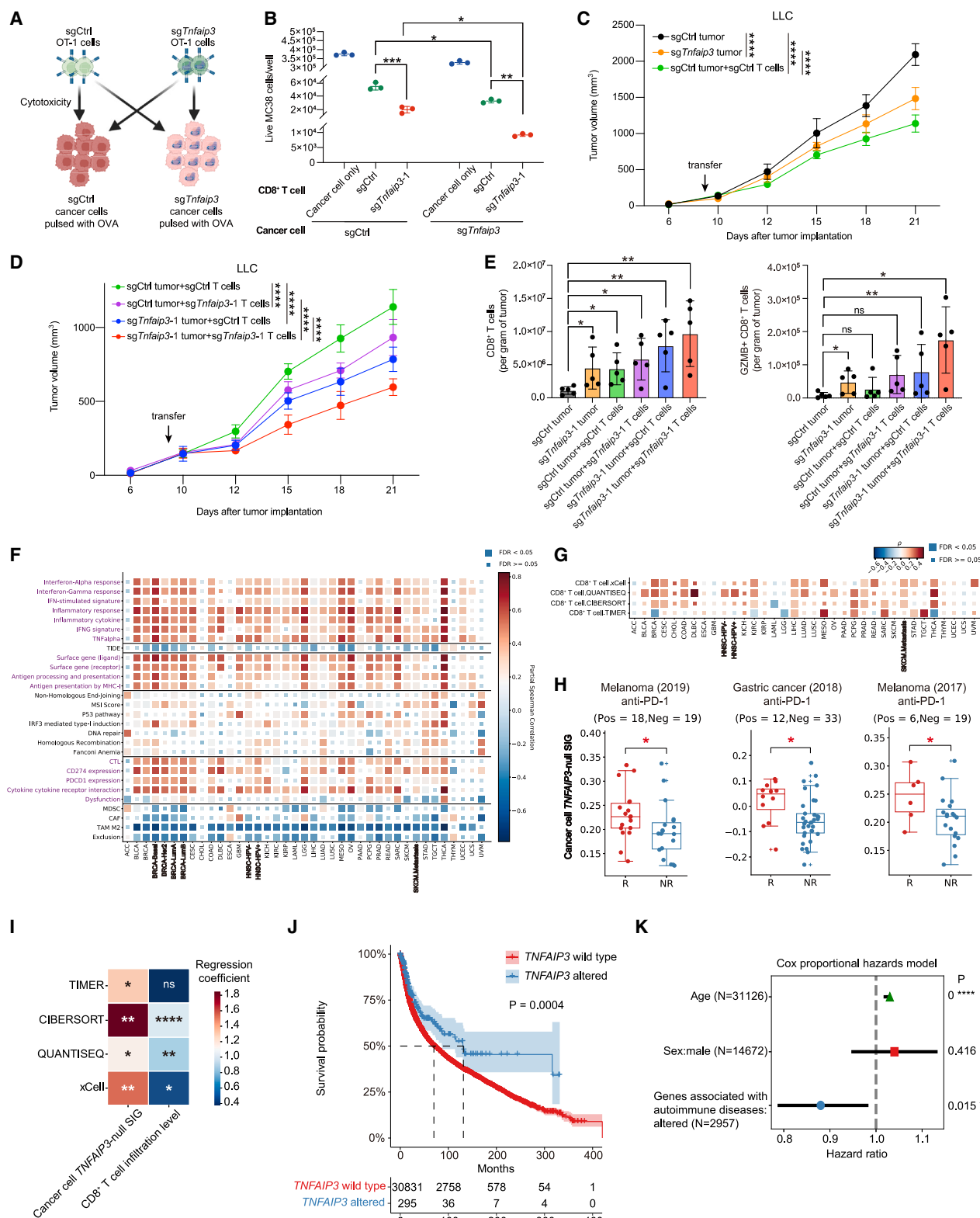**Figure 6. Combined *TNFAIP3* depletion in both cancer cells and T cells amplifies anti-tumor immune response through dual effects**

(A) *In vitro* co-culture assay setup of sgCtrl or sg*Tnfaip3* primary OT-I T cells co-cultured with either sgCtrl or sg*Tnfaip3* MC38 cells pre-pulsed with OVA peptide (257–264 aa, SIINFEKL) for 3 h. Number of alive cancer cells was counted 24 h later using flow cytometry.

In vivo studies were conducted to evaluate the impact of *Tnfaip3* deletion on anti-tumor efficacy via adoptive T cell transfer. OVA-expressing LLC cells were subcutaneously engrafted into WT mice, followed by the administration of edited OT-I T cells (Figure 5K; see STAR Methods). Following the infusion of T cells, no significant autoimmune-related symptoms, such as weight loss, irritability, or diminished appetite, were observed. The administration of *Tnfaip3*-null T cells resulted in a significant deceleration of tumor growth compared with the mice receiving control-edited T cells (Figure 5L). Flow cytometry analysis revealed an enhanced infiltration of immune cells into the tumors in mice receiving *Tnfaip3*-null OT-I T cells, with an increase in both overall CD45$^+$ leukocytes and CD8$^+$ T cell populations (Figures 5M and 5N). Collectively, these results elucidate that the deletion of *Tnfaip3* in CD8$^+$ T cells not only enhances their tumor-killing capacity but also promotes the maintenance of a contingent of TILs.

Combined *Tnfaip3* deletion in both cancer cells and T cells enhances anti-tumor efficacy through dual effects

Given the anti-tumor benefits observed from the ablation of *Tnfaip3* in cancer and T cells individually, we next investigated the potential synergy arising from simultaneous *Tnfaip3* deletion in these two cell types. Through cross-co-culturing *Tnfaip3*-ablated or control-ablated cancer cells with *Tnfaip3*-edited or control-edited T cells, we discovered that dual *Tnfaip3* inactivation increased cancer cell vulnerability to T cell-mediated cytotoxicity (Figures 6A and 6B). Comparative gene expression analysis between *TNFAIP3*-null A549 cancer cells and *Tnfaip3*-null OT-I T cells revealed the upregulation of synergistic pathways, including NF-κB signaling (*NFKB2*), type 2 IFN signaling (*ISG15* and *NOS2*), and TNF signaling (*NFKBIA* and *CX3CL1*) (Figures S4A and S4B), indicating an increased anti-tumor immunity. This analysis also uncovered differential pathway regulation, with hepatocyte growth factor receptor (MET)signaling (*COL1A1* and *FN1*) preferentially upregulated in T cells but repressed in cancer cells (Figures S4A and S4C). Vice versa, chromosome organization pathway (*APC* and *NBN*) and *IFNGR1* were upregulated in cancer cells but downregulated in T cells (Figures S4A and S4D). To explore the dual effects of *Tnfaip3* ablation *in vivo*, *Tnfaip3*-null or control-edited LLC-OVA cells were subcutaneously injected into WT mice, followed by the adoptive transfer of *Tnfaip3*-edited or control-edited OT-I T cells (Figure S4E). Notably, *Tnfaip3* deletion in either cancer cells or T cells independently conferred a reduction in tumor growth, whereas simultaneous inactivation in both cell types elicited the strongest anti-tumor response (Figures 6C and 6D). This phenotype was supported by flow cytometry analysis, which revealed an augmentation in GZMB$^+$ CD8$^+$ T cell infiltration in mice bearing *Tnfaip3*-null tumors following the administration of *Tnfaip3*-null T cells (Figure 6E). Collectively, these data underscore Tnfaip3 as a dual-effect target in amplifying anti-tumor immunity.

Next, we explored the clinical relevance of TNFAIP3 expression across human cancers. *TNFAIP3*-null signature was generated based on differentially expressed genes following *TNFAIP3* ablation (Table S7; see STAR Methods). Analyses of RNA-seq data from the CCLE data[83] indicated associations between the *TNFAIP3*-null signature and several key pathways, including the p53 pathway, antigen processing and presentation, and cytokine-cytokine receptor interaction (Figure S4F). This signature was then evaluated using the TCGA datasets.[93] In most human cancer types, the *TNFAIP3*-null signature demonstrated positive correlations with inflammatory response, cytokines, antigen processing and presentation, and responses to TNF, IFN-γ, and IFN-α (Figure 6F). Conversely, the signature showed negative correlations with immunosuppressive indicators, including cancer-associated fibroblasts (CAFs) and M2-like tumor-associated macrophages (TAMs) (Figure 6F). Further correlation analysis with TCGA data revealed negative associations between *TNFAIP3*-null signature and genes such as *CACFD1*, *BRF1*, and *WFS1* (Figure S4G). At the protein level, positive correlations were observed with lymphocyte-specific protein tyrosine kinase (LCK), PD-L1, and spleen tyrosine kinase (SYK), while negative correlations were identified with E-cadherin (CDH1), androgen receptor (AR), HER2, and AKT (Figure S4H). Further examination of correlations between the *TNFAIP3*-null signature and CD8$^+$ T cell infiltration in TCGA bulk tumors revealed a robust positive correlation with CD8$^+$ T cell infiltration across various cancer types (Figure 6G; see STAR Methods). Our analysis across multiple cohorts in ICRAFT revealed that the presence of the *TNFAIP3*-null signature was associated with improved responses to ICB therapy (Figure 6H). To account

(B) Number of alive sgCtrl or sg*Tnfaip3* edited cancer cells after co-culturing with sg*Tnfaip3* or sgCtrl edited primary OT-I CD8$^+$ T cells. n = 3 per group.

(C and D) Tumor growth curves of sg*Tnfaip3* tumors and sg*Tnfaip3* primary CD8$^+$ T cell administration, individually or combined, with sgCtrl as the control, in wild-type C57BL/6 mice. SgCtrl or sg*Tnfaip3* LLC cells (1 × 10^6 cells) were subcutaneously injected into 8-week-old C57BL/6 mice. Edited CD8$^+$ T cells (3 × 10^6) were administered via tail vein injection 9 days after cancer cell inoculation. (n = 5 mice per group).

(E) Flow cytometry analysis of tumor-infiltrating CD8$^+$ T cells (left) and GZMB$^+$ CD8$^+$ T cells (right), with gating on CD45+ cells.

(F) Heatmap of partial Spearman correlations between *TNFAIP3*-null signature level and molecular phenotypes or pathway scores across TCGA cancer types.

(G) Heatmap of partial Spearman correlations between *TNFAIP3*-null signature level and inferred levels of CD8$^+$ T cell infiltration across TCGA cancer types.

(H) Comparison of *TNFAIP3*-null signature level between responders and non-responders in three clinical trial cohorts prior to ICB treatment.

(I) Heatmap of regression coefficients and *p* values. Regression coefficients and *p* values were derived from multivariable logistic regression models evaluating the association between the *TNFAIP3*-null signature and immunotherapy response, with CD8$^+$ T cell infiltration level included as a confounding variable. Cohort-specific effects were adjusted using dummy variables.

(J) Survival analysis of curated cancer cohorts was conducted using the Kaplan-Meier estimate based on *TNFAIP3* genotype. Log-rank *p* value was calculated for statistical significance.

(K) Forest plot of hazard ratios for cancer prognosis risk factors from the Cox proportional hazards analysis. Full results are available in Table S9.

ns, not significant, *$p < 0.05$, **$p < 0.01$, ***$p < 0.001$, and ****$p < 0.0001$ by two-way ANOVA (B–D), unpaired Student's t test (E), Wilcoxon test (H), multivariable logistic regression (I), and Cox proportional hazards analysis (K). Data are presented as mean ± SD and are representative of at least two independent experiments (B–E). See also Figure S4 and Tables S7, S8, and S9.

for the potential confounding effect of CD8$^+$ T cell infiltration, we performed multivariable logistic regression analyses, with CD8$^+$ T cell infiltration level as a confounding variable (see STAR Methods). These analyses confirmed that the association between the *TNFAIP3*-null signature and immunotherapy response remained significant after adjusting for CD8$^+$ T cell infiltration (Figure 6I; see STAR Methods).

We assessed the clinical significance of *TNFAIP3* alterations using cancer mutation data. Analysis of 24 cancer types from the TCGA dataset revealed five types of *TNFAIP3* alterations, each occurring at low frequencies (<5%) (Figure S4I). Most of these mutations were missense mutations, located at post-translational modification sites such as phosphorylation, acetylation, and ubiquitination (Figure S4J). Further analysis of the cBioPortal for Cancer Genomics[97] dataset, in which we curated *TNFAIP3* alteration profiles from 97 cohorts covering 31,127 patients (Table S8), revealed a prognosis benefit for patients with *TNFAIP3* alterations compared with those with WT *TNFAIP3* (Figure 6J). Investigation using the COSMIC-3D database[98] revealed the 127th phenylalanine within the deubiquitinase domain of TNFAIP3 as a mutation hotspot (Figure S4K), corresponding to the single nucleotide polymorphism rs2230926, which has been linked to various autoimmune disorders.[99] Based on this observation, we expanded our analysis to include a broader range of genes associated with autoimmune diseases, as reported in previous studies,[100–106] hypothesizing that alterations in autoimmune-related genes may be broadly associated with altered cancer prognosis (Table S8; see STAR Methods). In our curated datasets, alterations in 20 of these genes were observed (Table S8). Survival analysis using the Cox proportional hazards regression model, adjusted for key prognostic factors such as age, sex, race, and cancer type, revealed that alterations in these autoimmune disease-related genes are associated with a lower hazard ratio (HR < 1, p = 0.015) (Figure 6K; Table S9; see STAR Methods), suggesting an association between these alterations and an improved prognosis for cancer patients.

Beyond target prioritization, ICRAFT also facilitates the deprioritization of therapeutic candidates by evaluating their effects across diverse cellular contexts. As a use case, we identified gene targets whose deletion improves cancer cell sensitivity to immune-mediated killing but has detrimental effects on immune cells. For instance, the deletion of RELA and RNF31, key components of the NF-κB signaling pathway, enhanced cancer cell sensitivity to T cell-mediated killing (Figures 2B and S5A). However, their inactivation also impaired immune cell viability. Specifically, *RELA*-null cells underwent apoptosis due to reduced expression of anti-apoptotic genes such as *Bcl-xL*, *c-IAP1*, and *c-IAP2* (Figures S5B–S5E). Likewise, while *RNF31* ablation enhanced cancer cell susceptibility to CD8$^+$ T and NK cell-mediated killing, it also had detrimental effects on immune cell function both *in vitro* and *in vivo* (Figures S5F–S5J). These results underscore the critical role of RELA and RNF31 in immune cell maintenance and highlight their unsuitability as therapeutic targets.

DISCUSSION

Here, we present ICRAFT (https://icraft.pku-genomics.org/), a comprehensive web platform to streamline the prioritization of gene targets with immune-modulatory effects. ICRAFT harnesses immune-related CRISPR screen datasets to delineate connections between gene perturbations and tumor-immune phenotypes, further incorporating transcriptomic analyses from single-cell and ICB clinical trial outcomes to elucidate gene expression programs and their clinical implications. Using ICRAFT, we identified a variety of gene candidates with immune-modulatory effects, highlighting *TNFAIP3* as a leading target. Experimental validations substantiated a dual function for TNFAIP3, in both cancer cells and T cells, with both functions resulting in enhanced anti-tumor immunity. In addition to target prioritization, ICRAFT can also help deprioritize gene targets by assessing the effects of target deletion across different cell types. For example, a target that increases tumor killing in cancer cells but induces dysfunction in T cells may not be ideal for therapy. Additionally, ICRAFT enables deeper exploration of less understood biological processes, such as gene targets with dual roles in B cells or macrophages. ICRAFT therefore provides a resource for systematic identification of therapeutic targets in tumor immunity. This resource will continue to be curated, maintained, and updated with new immune-related CRISPR screen datasets, scRNA-seq data, and pre-treatment RNA-seq data from clinical trials.

Utilizing ICRAFT, we conducted integrative analyses to identify critical regulatory gene targets within cancer and T cells. These analyses highlighted *SOCS1*, *PTPN2*, and *TNFAIP3* as prominent targets across both cancer cells and T cells. The dual functionality of SOCS1 and PTPN2 in modulating both cancer and T cells is well-established.[88–92] Through experimental and computational analyses, we corroborated the dual role of TNFAIP3. Notably, a subset of the identified genes possessing dual roles in both cancer and T cells are implicated in the negative regulation of inflammatory and cytokine signaling pathways. Theoretically, the ablation of genes within these pathways could deactivate negative regulatory mechanisms, thereby enhancing inflammation-related pathways.[107–109] Clinically, targeting genes that exert dual effects could synergistically enhance the therapeutic outcome by sensitizing cancer cells to immune-mediated cytotoxicity while simultaneously increasing immune activations. This study represents a comprehensive analysis to systematically explore gene targets with dual functionalities across two distinct cell types, thereby establishing a paradigm for future investigations into genes possessing multifaceted roles across diverse cell types and phenotypes.

TNFAIP3 functions as a negative regulator of NF-κB activity and TNF-mediated cell death. The NF-κB pathway regulates the expression of anti-apoptotic and survival genes, as well as inflammatory pathways. *Tnfaip3*-null murine embryonic fibroblasts are hypersensitive to TNF-induced apoptosis, with levels of survival proteins Bcl-2, c-IAP1, and TRAF2 comparable to those in *Tnfaip3* WT cells.[110] This suggests that TNFAIP3 protects cells from apoptosis independent of survival protein synthesis. Additionally, *TNFAIP3* deficiency triggers both RIPK1 kinase-dependent and independent apoptosis. TNFAIP3 is recruited to the tumor necrosis factor receptor 1 (TNFR1) signaling complex (complex I), where it stabilizes the linear (M1) ubiquitin network, preventing TNF receptor-associated death domain (TRADD) or RIPK1 dissociation from complex I. Once dissociated, TRADD and RIPK1 interact with FADD and caspase-8 to form the cytosolic apoptosis complex,[48] as

confirmed by our data. TNFAIP3 also protects cells from apoptosis by deubiquitylating caspase-8 and from necroptosis by deubiquitylating RIPK3.[111,112] We found that *TNFAIP3*-null cells produce elevated levels of inflammatory factors and chemokines, such as *CCL2*, *CCL20*, and *CXCL2*, resulting in increased recruitment of T cells and monocytes to the tumor microenvironment. Excessive NF-κB activation in *TNFAIP3*-null T cells enhanced the production of inflammatory factors, while *TNFAIP3*-null cancer cells are also more sensitive to TNF-mediated killing. This further contributed to improved tumor control *in vivo*.

An inhibitor targeting the PTPN2-PTPN1 axis can sensitize cancer cells to IFN-γ and enhance immune cell activation, inducing robust anti-tumor immunity in mouse models of ICB-resistant cancer.[65] The success of the PTPN2 inhibitor has heightened our interest in exploring therapeutic strategies targeting TNFAIP3. The OTU domain of TNFAIP3 contains several druggable pockets, presenting opportunities for small molecule intervention. Additionally, cell-specific *TNFAIP3* deficiencies in B cells, dendritic cells, and macrophages exhibit diverse autoimmune phenotypes,[113–115] suggesting that targeting TNFAIP3 could provoke broad immune activation and offer clinical benefits for cancer patients, similar to those observed with the PTPN2-PTPN1 inhibitor.[65] Beyond small molecule drugs, innovative targeting strategies such as RNA interference (RNAi) and proteolysis targeting chimeras (PROTACs) present promising avenues for targeting TNFAIP3 in therapeutic interventions.[116,117]

Dysregulated inflammatory and cytokine pathways lead to autoimmune disorders.[52,118–121] Our genomics analysis revealed that *TNFAIP3* alterations enhance cancer prognosis. We propose that TNFAIP3 mediates a balance between immune activation and suppression, with certain alterations potentially inducing autoimmunity, yet at the same time reducing cancer susceptibility. Autoimmune diseases arise from an inappropriately activated immune system. While autoimmune reactions generally have a detrimental effect on human health, they may conversely mitigate the risk of cancer development, a hypothesis that warrants further investigation. In addition, comprehensive studies are needed to clarify the relationship between autoimmune-associated genetic variants and cancer prognosis. Moreover, strategically targeting genes associated with autoimmunity could represent an approach to activate the immune system against tumors in cancer patients, a concept that requires systematic exploration.

Limitations of the study

A limitation of this study is the potential for batch effects in the ICB RNA-seq data curated from various sources. To address this, we applied quantile normalization and ComBat,[122] proven methods for mitigating batch effects in transcriptomic datasets.[123] However, we acknowledge that batch effects cannot be completely eliminated. Therefore, gene expression comparisons are more reliable within individual studies than between different studies. Another limitation is the incomplete understanding of the TNFAIP3-TNIP1 complex's broader functions beyond TNF-induced apoptosis and NF-κB modulation. The structural details of the TNFAIP3-TNIP1 complex and its interactions with other molecules also remain unclear, highlighting the need for comprehensive biochemical studies to elucidate these mechanisms.

RESOURCE AVAILABILITY

Lead contact

Further information and requests for resources and additional data should be directed to and will be fulfilled by the lead contact, Zexian Zeng (zexianzeng@pku.edu.cn).

Materials availability

This study did not generate new unique reagents or specific biological material. The materials used and generated in this study are available in the "STAR Methods" section. The data and code of this study are publicly available and are described in the "data and code availability" section.

Data and code availability

The data and code used in this study are available from the following sources: CRISPR screen datasets were collected from the GEO database (https://www.ncbi.nlm.nih.gov/geo/) or generously provided by the respective authors. Metadata for screen comparisons in ICRAFT can be found in Table S1. Human scRNA-seq datasets were obtained from GEO (https://www.ncbi.nlm.nih.gov/geo/) and ArrayExpress (https://www.ebi.ac.uk/arrayexpress/). The accession numbers for these datasets are provided in Table S2. ICB clinical trial cohorts RNA-seq data with patient survival and immunotherapy response information were acquired from published studies, as detailed in Table S3. RNA-seq data of 1,208 cancer cell lines and proteomic data of 373 cancer cell lines were downloaded from the DepMap portal (https://depmap.org/portal/download/all/). Gene-dependency levels based on 1,095 CRISPR-Cas9 essentiality screen datasets were obtained from the DepMap 2023 Q2 release (https://depmap.org/portal/download/all/). Transcriptome data and clinical data for TCGA cohorts were obtained from the TCGA Data Portal (https://portal.gdc.cancer.gov/). Processed spatial transcriptomics data for the colorectal cancer and breast cancer samples were downloaded from the 10x Genomics website (https://www.10xgenomics.com/datasets/human-colorectal-cancer-whole-transcriptome-analysis-1-standard-1-2-0 and https://www.10xgenomics.com/resources/datasets/human-breast-cancer-ductal-carcinoma-in-situ-invasive-carcinoma-ffpe-1-standard-1-3-0). Processed gene expression data of pan-cancer CD8+ CTLs were acquired from GEO: GSE156728. Survival data and genotype information for 31,127 patients across 97 cancer cohorts were acquired via cBioPortal (https://www.cbioportal.org/).

The CRISPR screen data, scRNA-seq data, and ICB therapeutic RNA-seq data in this paper can be accessed through the ICRAFT web server: https://icraft.pku-genomics.org/. RNA-seq data in this study have been deposited in the NCBI GEO: GSE261915. The Python code for the crawler and parser developed for ICRAFT is accessible on GitHub (https://github.com/zenglab-pku/ICRAFT_A20_paper).

AUTHOR CONTRIBUTIONS

Conceptualization, C.L., D.P., Z.G., and Z. Zeng; methodology, C.L., R.Z., R.G., L.W., Z.G., D.P., and Z. Zeng; software, C.L., Y.H., Y.J., and P.Z.; formal analysis, C.L., R.Z., and R.G.; investigation, C.L., R.Z., R.G., L.W., T.X., Y.H., Y.J., Y.Z., P.Z., and X.L.; writing – original draft, C.L., R.Z., R.G., D.P., and Z. Zeng; writing – review and editing, C.L., R.Z., R.G., S.Y., W.Z., C.W., L.L., Q.P.-H., K.W.W., Z.G., D.P., and Z. Zeng; funding acquisition, D.P. and Z. Zeng; resources, C.L., R.Z., R.G., T.X., Z. Zhang, P.Z., X.L., D.L., Z.G., D.P.,

and Z. Zeng; data curation, C.L., L.W., Y.Z., Z.G., and D.L.; visualization, C.L., R.Z., and R.G.; and supervision, Z.G., D.P., and Z. Zeng.

STAR★METHODS

Detailed methods are provided in the online version of this paper and include the following:

- KEY RESOURCES TABLE
- EXPERIMENTAL MODEL AND STUDY PARTICIPANT DETAILS
  - Animal studies
  - Cell lines
- METHOD DETAILS
  - Generation of genetically ablated cancer cell lines and T cells
  - CD8^{+} T cell activation and proliferation experiments
  - sg*TNFAIP3* A549 or OT-1 cells bulk RNA-Seq samples preparation
  - CD8^{+} T cell cytokine production experiments
  - CD8^{+} T cell target killing experiments
  - Cell apoptosis staining assay
  - Mouse tumor inoculation experiments
  - Tumor-infiltrating lymphocyte analysis
  - Western blot analysis
  - Statistical analysis
- QUANTIFICATION AND STATISTICAL ANALYSIS
  - CRISPR screen dataset collection and preprocessing
  - Human single-cell RNA-Seq collection and preprocessing
  - ICB clinical trial cohort RNA-Seq data collection and preprocessing
  - CCLE data collection and preprocessing
  - TCGA cohort data processing
  - CRISPR screen datasets integration analysis
  - Analysis of gene expression in spatial transcriptomics datasets
  - Bioinformatics and statistical analysis
  - Collection of *TNFAIP3* mutation profile

SUPPLEMENTAL INFORMATION

Supplemental information can be found online at https://doi.org/10.1016/j.immuni.2025.02.007.

REFERENCES

1. Ansell, S.M., Lesokhin, A.M., Borrello, I., Halwani, A., Scott, E.C., Gutierrez, M., Schuster, S.J., Millenson, M.M., Cattry, D., Freeman, G.J., et al. (2015). PD-1 blockade with nivolumab in relapsed or refractory Hodgkin's lymphoma. N. Engl. J. Med. *372*, 311–319. https://doi.org/10.1056/NEJMoa1411087.

2. Xu-Monette, Z.Y., Zhou, J., and Young, K.H. (2018). PD-1 expression and clinical PD-1 blockade in B-cell lymphomas. Blood *131*, 68–83. https://doi.org/10.1182/blood-2017-07-740993.

3. Hodi, F.S., O'Day, S.J., McDermott, D.F., Weber, R.W., Sosman, J.A., Haanen, J.B., Gonzalez, R., Robert, C., Schadendorf, D., Hassel, J.C., et al. (2010). Improved survival with ipilimumab in patients with metasta-tic melanoma. N. Engl. J. Med. *363*, 711–723. https://doi.org/10.1056/NEJMoa1003466.

4. Valero, C., Lee, M., Hoen, D., Zehir, A., Berger, M.F., Seshan, V.E., Chan, T.A., and Morris, L.G.T. (2021). Response rates to anti-PD-1 immuno-therapy in microsatellite-stable solid tumors with 10 or more mutations per megabase. JAMA Oncol. *7*, 739–743. https://doi.org/10.1001/jamaoncol.2020.7684.

5. Yarchoan, M., Hopkins, A., and Jaffee, E.M. (2017). Tumor mutational burden and response rate to PD-1 inhibition. N. Engl. J. Med. *377*, 2500–2501. https://doi.org/10.1056/NEJMc1713444.

6. Sharma, P., Hu-Lieskovan, S., Wargo, J.A., and Ribas, A. (2017). Primary, adaptive, and acquired resistance to cancer immunotherapy. Cell *168*, 707–723. https://doi.org/10.1016/j.cell.2017.01.017.

7. Arora, S., Velichinskii, R., Lesh, R.W., Ali, U., Kubiak, M., Bansal, P., Borghaei, H., Edelman, M.J., and Boumber, Y. (2019). Existing and emerging biomarkers for immune checkpoint immunotherapy in solid tumors. Adv. Ther. *36*, 2638–2678. https://doi.org/10.1007/s12325-019-01051-z.

8. Boland, C.R., and Goel, A. (2010). Microsatellite instability in colorectal cancer. Gastroenterology *138*, 2073–2087.e3. https://doi.org/10.1053/j.gastro.2009.12.064.

9. André, T., Shiu, K.K., Kim, T.W., Jensen, B.V., Jensen, L.H., Punt, C., Smith, D., Garcia-Carbonero, R., Benavides, M., Gibbs, P., et al. (2020). Pembrolizumab in microsatellite-instability-high advanced colo-rectal cancer. N. Engl. J. Med. *383*, 2207–2218. https://doi.org/10.1056/NEJMoa2017699.

10. Llosa, N.J., Cruise, M., Tam, A., Wicks, E.C., Hechenbleikner, E.M., Taube, J.M., Blosser, R.L., Fan, H., Wang, H., Luber, B.S., et al. (2015). The vigorous immune microenvironment of microsatellite instable colon cancer is balanced by multiple counter-inhibitory checkpoints. Cancer Discov. *5*, 43–51. https://doi.org/10.1158/2159-8290.CD-14-0863.

11. Le, D.T., Uram, J.N., Wang, H., Bartlett, B.R., Kemberling, H., Eyring, A.D., Skora, A.D., Luber, B.S., Azad, N.S., Laheru, D., et al. (2015). PD-1 blockade in tumors with mismatch-repair deficiency. N. Engl. J. Med. *372*, 2509–2520. https://doi.org/10.1056/NEJMoa1500596.

12. Niknafs, N., Balan, A., Cherry, C., Hummelink, K., Monkhorst, K., Shao, X.M., Belcaid, Z., Marrone, K.A., Murray, J., Smith, K.N., et al. (2023). Persistent mutation burden drives sustained anti-tumor immune re-sponses. Nat. Med. *29*, 440–449. https://doi.org/10.1038/s41591-022-02163-w.

13. Jiang, P., Gu, S., Pan, D., Fu, J., Sahu, A., Hu, X., Li, Z., Traugh, N., Bu, X., Li, B., et al. (2018). Signatures of T cell dysfunction and exclusion predict cancer immunotherapy response. Nat. Med. *24*, 1550–1558. https://doi.org/10.1038/s41591-018-0136-1.

14. Zeng, Z., Gu, S.S., Wong, C.J., Yang, L., Ouardaoui, N., Li, D., Zhang, W., Brown, M., and Liu, X.S. (2022). Machine learning on syngeneic mouse tumor profiles to model clinical immunotherapy response. Sci. Adv. *8*, eabm8564. https://doi.org/10.1126/sciadv.abm8564.

15. June, C.H., O'Connor, R.S., Kawalekar, O.U., Ghassemi, S., and Milone, M.C. (2018). CAR T cell immunotherapy for human cancer. Science *359*, 1361–1365. https://doi.org/10.1126/science.aar6711.

16. Zhao, L., and Cao, Y.J. (2019). Engineered T cell therapy for cancer in the clinic. Front. Immunol. *10*, 2250. https://doi.org/10.3389/fimmu.2019.02250.

17. Foy, S.P., Jacoby, K., Bota, D.A., Hunter, T., Pan, Z., Stawiski, E., Ma, Y., Lu, W., Peng, S., Wang, C.L., et al. (2023). Non-viral precision T cell re-ceptor replacement for personalized cell therapy. Nature *615*, 687–696. https://doi.org/10.1038/s41586-022-05531-1.

18. Roth, T.L., Puig-Saus, C., Yu, R., Shifrut, E., Carnevale, J., Li, P.J., Hiatt, J., Saco, J., Krystofinski, P., Li, H., et al. (2018). Reprogramming human T cell function and specificity with non-viral genome targeting. Nature *559*, 405–409. https://doi.org/10.1038/s41586-018-0326-5.

19. Levin, A.M., Bates, D.L., Ring, A.M., Krieg, C., Lin, J.T., Su, L., Moraga, I., Raeber, M.E., Bowman, G.R., Novick, P., et al. (2012). Exploiting a natural

conformational switch to engineer an interleukin-2 'superkine'. Nature *484*, 529–533. https://doi.org/10.1038/nature10975.

20. Wolf, N.K., Blaj, C., Picton, L.K., Snyder, G., Zhang, L., Nicolai, C.J., Ndubaku, C.O., McWhirter, S.M., Garcia, K.C., and Raulet, D.H. (2022). Synergy of a STING agonist and an IL-2 superkine in cancer immunotherapy against MHC I-deficient and MHC I(+) tumors. Proc. Natl. Acad. Sci. USA *119*, e2200568119. https://doi.org/10.1073/pnas.2200568119.

21. Smyth, M.J., Cretney, E., Kershaw, M.H., and Hayakawa, Y. (2004). Cytokines in cancer immunity and immunotherapy. Immunol. Rev. *202*, 275–293. https://doi.org/10.1111/j.0105-2896.2004.00199.x.

22. Bonati, L., and Tang, L. (2021). Cytokine engineering for targeted cancer immunotherapy. Curr. Opin. Chem. Biol. *62*, 43–52. https://doi.org/10.1016/j.cbpa.2021.01.007.

23. Rohaan, M.W., Borch, T.H., van den Berg, J.H., Met, O., Kessels, R., Geukes Foppen, M.H., Stoltenborg Granhoj, J., Nuijen, B., Nijenhuis, C., Jedema, I., et al. (2022). Tumor-Infiltrating Lymphocyte Therapy or Ipilimumab in Advanced Melanoma. N. Engl. J. Med. *387*, 2113–2125. https://doi.org/10.1056/NEJMoa2210233.

24. Stadtmauer, E.A., Fraietta, J.A., Davis, M.M., Cohen, A.D., Weber, K.L., Lancaster, E., Mangan, P.A., Kulikovskaya, I., Gupta, M., Chen, F., et al. (2020). CRISPR-engineered T cells in patients with refractory cancer. Science *367*, eaba7365. https://doi.org/10.1126/science.aba7365.

25. Kumar, S., Zeng, Z., Bagati, A., Tay, R.E., Sanz, L.A., Hartono, S.R., Ito, Y., Abderazzaq, F., Hatchi, E., Jiang, P., et al. (2021). CARM1 inhibition enables immunotherapy of resistant tumors by dual action on tumor cells and T cells. Cancer Discov. *11*, 2050–2071. https://doi.org/10.1158/2159-8290.CD-20-1144.

26. Wu, L., Jin, Y., Zhao, X., Tang, K., Zhao, Y., Tong, L., Yu, X., Xiong, K., Luo, C., Zhu, J., et al. (2023). Tumor aerobic glycolysis confers immune evasion through modulating sensitivity to T cell-mediated bystander killing via TNF-alpha. Cell Metab. *35*, 1580–1596.e9. https://doi.org/10.1016/j.cmet.2023.07.001.

27. Pardoll, D.M. (2012). The blockade of immune checkpoints in cancer immunotherapy. Nat. Rev. Cancer *12*, 252–264. https://doi.org/10.1038/nrc3239.

28. Sharma, P., and Allison, J.P. (2015). Immune checkpoint targeting in cancer therapy: toward combination strategies with curative potential. Cell *161*, 205–214. https://doi.org/10.1016/j.cell.2015.03.030.

29. Dong, M.B., Tang, K., Zhou, X., Zhou, J.J., and Chen, S. (2022). Tumor immunology CRISPR screening: present, past, and future. Trends Cancer *8*, 210–225. https://doi.org/10.1016/j.trecan.2021.11.009.

30. Shi, H., Doench, J.G., and Chi, H. (2023). CRISPR screens for functional interrogation of immunity. Nat. Rev. Immunol. *23*, 363–380. https://doi.org/10.1038/s41577-022-00802-4.

31. Pan, D., Kobayashi, A., Jiang, P., Ferrari de Andrade, L., Tay, R.E., Luoma, A.M., Tsoucas, D., Qiu, X., Lim, K., Rao, P., et al. (2018). A major chromatin regulator determines resistance of tumor cells to T cell-mediated killing. Science *359*, 770–775. https://doi.org/10.1126/science.aao1710.

32. Larson, R.C., Kann, M.C., Bailey, S.R., Haradhvala, N.J., Llopis, P.M., Bouffard, A.A., Scarfó, I., Leick, M.B., Grauwet, K., Berger, T.R., et al. (2022). CAR T cell killing requires the IFNgammaR pathway in solid but not liquid tumours. Nature *604*, 563–570. https://doi.org/10.1038/s41586-022-04585-5.

33. Manguso, R.T., Pope, H.W., Zimmer, M.D., Brown, F.D., Yates, K.B., Miller, B.C., Collins, N.B., Bi, K., LaFleur, M.W., Juneja, V.R., et al. (2017). In vivo CRISPR screening identifies Ptpn2 as a cancer immunotherapy target. Nature *547*, 413–418. https://doi.org/10.1038/nature23270.

34. Ishizuka, J.J., Manguso, R.T., Cheruiyot, C.K., Bi, K., Panda, A., Iracheta-Vellve, A., Miller, B.C., Du, P.P., Yates, K.B., Dubrot, J., et al. (2019). Loss of ADAR1 in tumours overcomes resistance to immune checkpoint blockade. Nature *565*, 43–48. https://doi.org/10.1038/s41586-018-0768-9.

35. Wang, X., Tokheim, C., Gu, S.S., Wang, B., Tang, Q., Li, Y., Traugh, N., Zeng, Z., Zhang, Y., Li, Z., et al. (2021). In vivo CRISPR screens identify the E3 ligase Cop1 as a modulator of macrophage infiltration and cancer immunotherapy target. Cell *184*, 5357–5374.e22. https://doi.org/10.1016/j.cell.2021.09.006.

36. Griffin, G.K., Wu, J., Iracheta-Vellve, A., Patti, J.C., Hsu, J., Davis, T., Dele-Oni, D., Du, P.P., Halawi, A.G., Ishizuka, J.J., et al. (2021). Epigenetic silencing by SETDB1 suppresses tumour intrinsic immunogenicity. Nature *595*, 309–314. https://doi.org/10.1038/s41586-021-03520-4.

37. Shifrut, E., Carnevale, J., Tobin, V., Roth, T.L., Woo, J.M., Bui, C.T., Li, P.J., Diolaiti, M.E., Ashworth, A., and Marson, A. (2018). Genome-wide CRISPR screens in primary human T cells reveal key regulators of immune function. Cell *175*, 1958–1971.e15. https://doi.org/10.1016/j.cell.2018.10.024.

38. Schmidt, R., Steinhart, Z., Layeghi, M., Freimer, J.W., Bueno, R., Nguyen, V.Q., Blaeschke, F., Ye, C.J., and Marson, A. (2022). CRISPR activation and interference screens decode stimulation responses in primary human T cells. Science *375*, eabj4008. https://doi.org/10.1126/science.abj4008.

39. Freimer, J.W., Shaked, O., Naqvi, S., Sinnott-Armstrong, N., Kathiria, A., Garrido, C.M., Chen, A.F., Cortez, J.T., Greenleaf, W.J., Pritchard, J.K., et al. (2022). Systematic discovery and perturbation of regulatory genes in human T cells reveals the architecture of immune networks. Nat. Genet. *54*, 1133–1144. https://doi.org/10.1038/s41588-022-01106-y.

40. Freitas, K.A., Belk, J.A., Sotillo, E., Quinn, P.J., Ramello, M.C., Malipatlolla, M., Daniel, B., Sandor, K., Klysz, D., Bjelajac, J., et al. (2022). Enhanced T cell effector activity by targeting the Mediator kinase module. Science *378*, eabn5647. https://doi.org/10.1126/science.abn5647.

41. Schmidt, R., Ward, C.C., Dajani, R., Armour-Garb, Z., Ota, M., Allain, V., Hernandez, R., Layeghi, M., Xing, G., Goudy, L., et al. (2024). Base-editing mutagenesis maps alleles to tune human T cell functions. Nature *625*, 805–812. https://doi.org/10.1038/s41586-023-06835-6.

42. Belk, J.A., Yao, W., Ly, N., Freitas, K.A., Chen, Y.T., Shi, Q., Valencia, A.M., Shifrut, E., Kale, N., Yost, K.E., et al. (2022). Genome-wide CRISPR screens of T cell exhaustion identify chromatin remodeling factors that limit T cell persistence. Cancer Cell *40*, 768–786.e7. https://doi.org/10.1016/j.ccell.2022.06.001.

43. Wu, J.E., Manne, S., Ngiow, S.F., Baxter, A.E., Huang, H., Freilich, E., Clark, M.L., Lee, J.H., Chen, Z., Khan, O., et al. (2023). In vitro modeling of CD8(+) T cell exhaustion enables CRISPR screening to reveal a role for BHLHE40. Sci. Immunol. *8*, eade3369. https://doi.org/10.1126/sciimmunol.ade3369.

44. Carnevale, J., Shifrut, E., Kale, N., Nyberg, W.A., Blaeschke, F., Chen, Y.Y., Li, Z., Bapat, S.P., Diolaiti, M.E., O'Leary, P., et al. (2022). RASA2 ablation in T cells boosts antigen sensitivity and long-term function. Nature *609*, 174–182. https://doi.org/10.1038/s41586-022-05126-w.

45. Wertz, I.E., O'Rourke, K.M., Zhou, H., Eby, M., Aravind, L., Seshagiri, S., Wu, P., Wiesmann, C., Baker, R., Boone, D.L., et al. (2004). De-ubiquitination and ubiquitin ligase domains of A20 downregulate NF-kappaB signalling. Nature *430*, 694–699. https://doi.org/10.1038/nature02794.

46. Mauro, C., Pacifico, F., Lavorgna, A., Mellone, S., Iannetti, A., Acquaviva, R., Formisano, S., Vito, P., and Leonardi, A. (2006). ABIN-1 binds to NEMO/IKKgamma and co-operates with A20 in inhibiting NF-kappaB. J. Biol. Chem. *281*, 18482–18488. https://doi.org/10.1074/jbc.M601502200.

47. Düwel, M., Welteke, V., Oeckinghaus, A., Baens, M., Kloo, B., Ferch, U., Darnay, B.G., Ruland, J., Marynen, P., and Krappmann, D. (2009). A20 negatively regulates T cell receptor signaling to NF-kappaB by cleaving Malt1 ubiquitin chains. J. Immunol. *182*, 7718–7728. https://doi.org/10.4049/jimmunol.0803313.

48. Priem, D., Devos, M., Druwé, S., Martens, A., Slowicka, K., Ting, A.T., Pasparakis, M., Declercq, W., Vandenabeele, P., van Loo, G., et al. (2019). A20 protects cells from TNF-induced apoptosis through linear

ubiquitin-dependent and -independent mechanisms. Cell Death Dis. *10*, 692. https://doi.org/10.1038/s41419-019-1937-y.

49. Parvatiyar, K., Barber, G.N., and Harhaj, E.W. (2010). TAX1BP1 and A20 inhibit antiviral signaling by targeting TBK1-IKKi kinases. J. Biol. Chem. *285*, 14999–15009. https://doi.org/10.1074/jbc.M110.109819.

50. Matsuzawa, Y., Oshima, S., Takahara, M., Maeyashiki, C., Nemoto, Y., Kobayashi, M., Nibe, Y., Nozaki, K., Nagaishi, T., Okamoto, R., et al. (2015). TNFAIP3 promotes survival of CD4 T cells by restricting MTOR and promoting autophagy. Autophagy *11*, 1052–1062. https://doi.org/10.1080/15548627.2015.1055439.

51. Priem, D., van Loo, G., and Bertrand, M.J.M. (2020). A20 and cell death-driven inflammation. Trends Immunol. *41*, 421–435. https://doi.org/10.1016/j.it.2020.03.001.

52. Martens, A., and van Loo, G. (2020). A20 at the crossroads of cell death, inflammation, and autoimmunity. Cold Spring Harb. Perspect. Biol. *12*, a036418. https://doi.org/10.1101/cshperspect.a036418.

53. Ma, A., and Malynn, B.A. (2012). A20: linking a complex regulator of ubiquitylation to immunity and human disease. Nat. Rev. Immunol. *12*, 774–785. https://doi.org/10.1038/nri3313.

54. Zhou, Q., Wang, H., Schwartz, D.M., Stoffels, M., Park, Y.H., Zhang, Y., Yang, D., Demirkaya, E., Takeuchi, M., Tsai, W.L., et al. (2016). Loss-of-function mutations in TNFAIP3 leading to A20 haploinsufficiency cause an early-onset autoinflammatory disease. Nat. Genet. *48*, 67–73. https://doi.org/10.1038/ng.3459.

55. Compagno, M., Lim, W.K., Grunn, A., Nandula, S.V., Brahmachary, M., Shen, Q., Bertoni, F., Ponzoni, M., Scandurra, M., Califano, A., et al. (2009). Mutations of multiple genes cause deregulation of NF-kappaB in diffuse large B-cell lymphoma. Nature *459*, 717–721. https://doi.org/10.1038/nature07968.

56. Ren, W., Wang, X., Yang, M., Wan, H., Li, X., Ye, X., Meng, B., Li, W., Yu, J., Lei, M., et al. (2022). Distinct clinical and genetic features of hepatitis B virus-associated follicular lymphoma in Chinese patients. Blood Adv. *6*, 2731–2744. https://doi.org/10.1182/bloodadvances.2021006410.

57. Schmitz, R., Wright, G.W., Huang, D.W., Johnson, C.A., Phelan, J.D., Wang, J.Q., Roulland, S., Kasbekar, M., Young, R.M., Shaffer, A.L., et al. (2018). Genetics and pathogenesis of diffuse large B-cell lymphoma. N. Engl. J. Med. *378*, 1396–1407. https://doi.org/10.1056/NEJMoa1801445.

58. Chen, C., Chen, Z., Huang, L., Zhou, L., Zhu, L., Liu, S., Luo, G., Li, W., Zeng, C., and Li, Y. (2021). TNFAIP3 mutation may be associated with favorable overall survival for patients with T-cell lymphoma. Cancer Cell Int. *21*, 490. https://doi.org/10.1186/s12935-021-02191-5.

59. Luo, M., Wang, X., Wu, S., Yang, C., Su, Q., Huang, L., Fu, K., An, S., Xie, F., To, K.K.W., et al. (2023). A20 promotes colorectal cancer immune evasion by upregulating STC1 expression to block "eat-me" signal. Signal Transduct. Target. Ther. *8*, 312. https://doi.org/10.1038/s41392-023-01545-x.

60. Breitenecker, K., Homolya, M., Luca, A.C., Lang, V., Trenk, C., Petroczi, G., Mohrherr, J., Horvath, J., Moritsch, S., Haas, L., et al. (2021). Down-regulation of A20 promotes immune escape of lung adenocarcinomas. Sci. Transl. Med. *13*, eabc3911. https://doi.org/10.1126/scitranslmed.abc3911.

61. Guo, W., Ma, J., Guo, S., Wang, H., Wang, S., Shi, Q., Liu, L., Zhao, T., Yang, F., Chen, S., et al. (2020). A20 regulates the therapeutic effect of anti-PD-1 immunotherapy in melanoma. J. Immunother. Cancer *8*, e001866. https://doi.org/10.1136/jitc-2020-001866.

62. Wiede, F., Lu, K.H., Du, X., Liang, S., Hochheiser, K., Dodd, G.T., Goh, P.K., Kearney, C., Meyran, D., Beavis, P.A., et al. (2020). PTPN2 phosphatase deletion in T cells promotes anti-tumour immunity and CAR T-cell efficacy in solid tumours. EMBO J. *39*, e103637. https://doi.org/10.15252/embj.2019103637.

63. LaFleur, M.W., Nguyen, T.H., Coxe, M.A., Miller, B.C., Yates, K.B., Gillis, J.E., Sen, D.R., Gaudiano, E.F., Al Abosy, R., Freeman, G.J., et al. (2019). PTPN2 regulates the generation of exhausted CD8(+) T cell subpopula-

tions and restrains tumor immunity. Nat. Immunol. *20*, 1335–1347. https://doi.org/10.1038/s41590-019-0480-4.

64. Flosbach, M., Oberle, S.G., Scherer, S., Zecha, J., von Hoesslin, M., Wiede, F., Chennupati, V., Cullen, J.G., List, M., Pauling, J.K., et al. (2020). PTPN2 deficiency enhances programmed T cell expansion and survival capacity of activated T cells. Cell Rep. *32*, 107957. https://doi.org/10.1016/j.celrep.2020.107957.

65. Baumgartner, C.K., Ebrahimi-Nik, H., Iracheta-Vellve, A., Hamel, K.M., Olander, K.E., Davis, T.G.R., McGuire, K.A., Halvorsen, G.T., Avila, O.I., Patel, C.H., et al. (2023). The PTPN2/PTPN1 inhibitor ABBV-CLS-484 unleashes potent anti-tumour immunity. Nature *622*, 850–862. https://doi.org/10.1038/s41586-023-06575-7.

66. Zitzmann, K., Brand, S., De Toni, E.N., Baehs, S., Göke, B., Meinecke, J., Spöttl, G., Meyer, H.H.H.D., and Auernhammer, C.J. (2007). SOCS1 silencing enhances antitumor activity of type I IFNs by regulating apoptosis in neuroendocrine tumor cells. Cancer Res. *67*, 5025–5032. https://doi.org/10.1158/0008-5472.CAN-06-2575.

67. Sutra Del Galy, A., Menegatti, S., Fuentealba, J., Lucibello, F., Perrin, L., Helft, J., Darbois, A., Saitakis, M., Tosello, J., Rookhuizen, D., et al. (2021). In vivo genome-wide CRISPR screens identify SOCS1 as intrinsic checkpoint of CD4(+) T(H)1 cell response. Sci. Immunol. *6*, eabe8219. https://doi.org/10.1126/sciimmunol.abe8219.

68. Davis, M.M., Boniface, J.J., Reich, Z., Lyons, D., Hampl, J., Arden, B., and Chien, Y. (1998). Ligand recognition by alpha beta T cell receptors. Annu. Rev. Immunol. *16*, 523–544. https://doi.org/10.1146/annurev.immunol.16.1.523.

69. Gu, S.S., Zhang, W., Wang, X., Jiang, P., Traugh, N., Li, Z., Meyer, C., Stewig, B., Xie, Y., Bu, X., et al. (2021). Therapeutically increasing MHC-I expression potentiates immune checkpoint blockade. Cancer Discov. *11*, 1524–1541. https://doi.org/10.1158/2159-8290.CD-20-0812.

70. Sharpe, A.H., Wherry, E.J., Ahmed, R., and Freeman, G.J. (2007). The function of programmed cell death 1 and its ligands in regulating autoimmunity and infection. Nat. Immunol. *8*, 239–245. https://doi.org/10.1038/ni1443.

71. Greenwald, R.J., Freeman, G.J., and Sharpe, A.H. (2005). The B7 family revisited. Annu. Rev. Immunol. *23*, 515–548. https://doi.org/10.1146/annurev.immunol.23.021704.115611.

72. Chen, L. (2004). Co-inhibitory molecules of the B7-CD28 family in the control of T-cell immunity. Nat. Rev. Immunol. *4*, 336–347. https://doi.org/10.1038/nri1349.

73. Tumeh, P.C., Harview, C.L., Yearley, J.H., Shintaku, I.P., Taylor, E.J.M., Robert, L., Chmielowski, B., Spasic, M., Henry, G., Ciobanu, V., et al. (2014). PD-1 blockade induces responses by inhibiting adaptive immune resistance. Nature *515*, 568–571. https://doi.org/10.1038/nature13954.

74. Daud, A.I., Loo, K., Pauli, M.L., Sanchez-Rodriguez, R., Sandoval, P.M., Taravati, K., Tsai, K., Nosrati, A., Nardo, L., Alvarado, M.D., et al. (2016). Tumor immune profiling predicts response to anti-PD-1 therapy in human melanoma. J. Clin. Invest. *126*, 3447–3452. https://doi.org/10.1172/JCI87324.

75. Chiang, Y.J., Kole, H.K., Brown, K., Naramura, M., Fukuhara, S., Hu, R.J., Jang, I.K., Gutkind, J.S., Shevach, E., and Gu, H. (2000). Cbl-b regulates the CD28 dependence of T-cell activation. Nature *403*, 216–220. https://doi.org/10.1038/35003235.

76. Mérida, I., Andrada, E., Gharbi, S.I., and Ávila-Flores, A. (2015). Redundant and specialized roles for diacylglycerol kinases alpha and zeta in the control of T cell functions. Sci. Signal. *8*, re6. https://doi.org/10.1126/scisignal.aaa0974.

77. Kolde, R., Laur, S., Adler, P., and Vilo, J. (2012). Robust rank aggregation for gene list integration and meta-analysis. Bioinformatics *28*, 573–580. https://doi.org/10.1093/bioinformatics/btr709.

78. Zaretsky, J.M., Garcia-Diaz, A., Shin, D.S., Escuin-Ordinas, H., Hugo, W., Hu-Lieskovan, S., Torrejon, D.Y., Abril-Rodriguez, G., Sandoval, S., Barthly, L., et al. (2016). Mutations associated with acquired resistance to PD-1 blockade in melanoma. N. Engl. J. Med. *375*, 819–829. https://doi.org/10.1056/NEJMoa1604958.

79. Vredevoogd, D.W., Kuilman, T., Ligtenberg, M.A., Boshuizen, J., Stecker, K.E., de Bruijn, B., Krijgsman, O., Huang, X., Kenski, J.C.N., Lacroix, R., et al. (2019). Augmenting immunotherapy impact by lowering tumor TNF cytotoxicity threshold. Cell 178, 585–599.e15. https://doi.org/10.1016/j.cell.2019.06.014.

80. Steinert, E.M., Vasan, K., and Chandel, N.S. (2021). Mitochondrial metabolism regulation of T cell-mediated immunity. Annu. Rev. Immunol. 39, 395–416. https://doi.org/10.1146/annurev-immunol-101819-082015.

81. Vardhana, S.A., Hwee, M.A., Berisa, M., Wells, D.K., Yost, K.E., King, B., Smith, M., Herrera, P.S., Chang, H.Y., Satpathy, A.T., et al. (2020). Impaired mitochondrial oxidative phosphorylation limits the self-renewal of T cells exposed to persistent antigen. Nat. Immunol. 21, 1022–1033. https://doi.org/10.1038/s41590-020-0725-2.

82. Martin, E., Palmic, N., Sanquer, S., Lenoir, C., Hauck, F., Mongellaz, C., Fabrega, S., Nitschke, P., Esposti, M.D., Schwartzentruber, J., et al. (2014). CTP synthase 1 deficiency in humans reveals its central role in lymphocyte proliferation. Nature 510, 288–292. https://doi.org/10.1038/nature13386.

83. Behan, F.M., Iorio, F., Picco, G., Gonçalves, E., Beaver, C.M., Migliardi, G., Santos, R., Rao, Y., Sassi, F., Pinnelli, M., et al. (2019). Prioritization of cancer therapeutic targets using CRISPR-Cas9 screens. Nature 568, 511–516. https://doi.org/10.1038/s41586-019-1103-9.

84. Qin, Q., Fan, J., Zheng, R., Wan, C., Mei, S., Wu, Q., Sun, H., Brown, M., Zhang, J., Meyer, C.A., et al. (2020). Lisa: inferring transcriptional regulators through integrative modeling of public chromatin accessibility and ChIP-seq data. Genome Biol. 21, 32. https://doi.org/10.1186/s13059-020-1934-6.

85. Roebuck, K.A., and Finnegan, A. (1999). Regulation of intercellular adhesion molecule-1 (CD54) gene expression. J. Leukoc. Biol. 66, 876–888. https://doi.org/10.1002/jlb.66.6.876.

86. Shirey, K.A., Jung, J.Y., Maeder, G.S., and Carlin, J.M. (2006). Upregulation of IFN-gamma receptor expression by proinflammatory cytokines influences IDO activation in epithelial cells. J. Interferon Cytokine Res. 26, 53–62. https://doi.org/10.1089/jir.2006.26.53.

87. Liu, T., Zhang, L., Joo, D., and Sun, S.C. (2017). NF-kappaB signaling in inflammation. Signal Transduct. Target. Ther. 2, 17023. https://doi.org/10.1038/sigtrans.2017.23.

88. Heyninck, K., De Valck, D., Vanden Berghe, W., Van Criekinge, W., Contreras, R., Fiers, W., Haegeman, G., and Beyaert, R. (1999). The zinc finger protein A20 inhibits TNF-induced NF-kappaB-dependent gene expression by interfering with an RIP- or TRAF2-mediated transactivation signal and directly binds to a novel NF-kappaB-inhibiting protein ABIN. J. Cell Biol. 145, 1471–1482. https://doi.org/10.1083/jcb.145.7.1471.

89. Heyninck, K., Kreike, M.M., and Beyaert, R. (2003). Structure-function analysis of the A20-binding inhibitor of NF-kappa B activation, ABIN-1. FEBS Lett. 536, 135–140. https://doi.org/10.1016/s0014-5793(03)00041-3.

90. Verstrepen, L., Carpentier, I., Verhelst, K., and Beyaert, R. (2009). ABINs: A20 binding inhibitors of NF-kappa B and apoptosis signaling. Biochem. Pharmacol. 78, 105–114. https://doi.org/10.1016/j.bcp.2009.02.009.

91. Lei, Q., Gu, H., Li, L., Wu, T., Xie, W., Li, M., and Zhao, N. (2020). TNIP1-mediated TNF-alpha/NF-kappaB signalling cascade sustains glioma cell proliferation. J. Cell. Mol. Med. 24, 530–538. https://doi.org/10.1111/jcmm.14760.

92. Yin, H., Karayel, O., Chao, Y.Y., Seeholzer, T., Hamp, I., Plettenburg, O., Gehring, T., Zielinski, C., Mann, M., and Krappmann, D. (2022). A20 and ABIN-1 cooperate in balancing CBM complex-triggered NF-kappaB signaling in activated T cells. Cell. Mol. Life Sci. 79, 112. https://doi.org/10.1007/s00018-022-04154-z.

93. Cancer; Genome; Atlas; Research Network, Weinstein, J.N., Collisson, E.A., Mills, G.B., Shaw, K.R.M., Ozenberger, B.A., Ellrott, K., Shmulevich, I., Sander, C., and Stuart, J.M. (2013). The Cancer Genome Atlas Pan-Cancer analysis project. Nat. Genet. 45, 1113–1120. https://doi.org/10.1038/ng.2764.

94. Uhlen, M., Karlsson, M.J., Zhong, W., Tebani, A., Pou, C., Mikes, J., Lakshmikanth, T., Forsström, B., Edfors, F., Odeberg, J., et al. (2019). A genome-wide transcriptomic analysis of protein-coding genes in human blood cells. Science 366, eaax9198. https://doi.org/10.1126/science.aax9198.

95. Zheng, L., Qin, S., Si, W., Wang, A., Xing, B., Gao, R., Ren, X., Wang, L., Wu, X., Zhang, J., et al. (2021). Pan-cancer single-cell landscape of tumor-infiltrating T cells. Science 374, abe6474. https://doi.org/10.1126/science.abe6474.

96. Gray, S.M., Amezquita, R.A., Guan, T., Kleinstein, S.H., and Kaech, S.M. (2017). Polycomb repressive complex 2-mediated chromatin repression guides effector CD8(+) T cell terminal differentiation and loss of multipotency. Immunity 46, 596–608. https://doi.org/10.1016/j.immuni.2017.03.012.

97. Cerami, E., Gao, J., Dogrusoz, U., Gross, B.E., Sumer, S.O., Aksoy, B.A., Jacobsen, A., Byrne, C.J., Heuer, M.L., Larsson, E., et al. (2012). The cBio cancer genomics portal: an open platform for exploring multidimensional cancer genomics data. Cancer Discov. 2, 401–404. https://doi.org/10.1158/2159-8290.CD-12-0095.

98. Jubb, H.C., Saini, H.K., Verdonk, M.L., and Forbes, S.A. (2018). COSMIC-3D provides structural perspectives on cancer genetics for drug discovery. Nat. Genet. 50, 1200–1202. https://doi.org/10.1038/s41588-018-0214-9.

99. Musone, S.L., Taylor, K.E., Lu, T.T., Nititham, J., Ferreira, R.C., Ortmann, W., Shifrin, N., Petri, M.A., Kamboh, M.I., Manzi, S., et al. (2008). Multiple polymorphisms in the TNFAIP3 region are independently associated with systemic lupus erythematosus. Nat. Genet. 40, 1062–1064. https://doi.org/10.1038/ng.202.

100. Szekanecz, Z., McInnes, I.B., Schett, G., Szamosi, S., Benkő, S., and Szűcs, G. (2021). Autoinflammation and autoimmunity across rheumatic and musculoskeletal diseases. Nat. Rev. Rheumatol. 17, 585–595. https://doi.org/10.1038/s41584-021-00652-9.

101. Touitou, I., and Koné-Paut, I. (2008). Autoinflammatory diseases. Best Pract. Res. Clin. Rheumatol. 22, 811–829. https://doi.org/10.1016/j.berh.2008.08.009.

102. Yang, C.A., and Chiang, B.L. (2015). Inflammasomes and human autoimmunity: A comprehensive review. J. Autoimmun. 61, 1–8. https://doi.org/10.1016/j.jaut.2015.05.001.

103. Lorenzini, T., Dotta, L., Giacomelli, M., Vairo, D., and Badolato, R. (2017). STAT mutations as program switchers: turning primary immunodeficiencies into autoimmune diseases. J. Leukoc. Biol. 101, 29–38. https://doi.org/10.1189/jlb.5RI0516-237RR.

104. Aricò, M., Boggio, E., Cetica, V., Melensi, M., Orilieri, E., Clemente, N., Cappellano, G., Buttini, S., Soluri, M.F., Comi, C., et al. (2013). Variations of the UNC13D gene in patients with autoimmune lymphoproliferative syndrome. PLoS One 8, e68045. https://doi.org/10.1371/journal.pone.0068045.

105. Rieux-Laucat, F., Magérus-Chatinet, A., and Neven, B. (2018). The autoimmune lymphoproliferative syndrome with defective FAS or FAS-ligand functions. J. Clin. Immunol. 38, 558–568. https://doi.org/10.1007/s10875-018-0523-x.

106. Baysac, K., Sun, G., Nakano, H., Schmitz, E.G., Cruz, A.C., Fisher, C., Bailey, A.C., Mace, E., Milner, J.D., et al.; PLCG2-Immune; Dysregulation Working Group (2024). PLCG2-associated immune dysregulation (PLAID) comprises broad and distinct clinical presentations related to functional classes of genetic variants. J. Allergy Clin. Immunol. 153, 230–242. https://doi.org/10.1016/j.jaci.2023.08.036.

107. Verzella, D., Pescatore, A., Capece, D., Vecchiotti, D., Ursini, M.V., Franzoso, G., Alesse, E., and Zazzeroni, F. (2020). Life, death, and autophagy in cancer: NF-kappaB turns up everywhere. Cell Death Dis. 11, 210. https://doi.org/10.1038/s41419-020-2399-y.

108. Barnes, S.E., Wang, Y., Chen, L., Molinero, L.L., Gajewski, T.F., Evaristo, C., and Alegre, M.L. (2015). T cell-NF-kappaB activation is required for tumor control in vivo. J. Immunother. Cancer 3, 1. https://doi.org/10.1186/s40425-014-0045-x.

109. Klein, K., He, K., Younes, A.I., Barsoumian, H.B., Chen, D., Ozgen, T., Mosaffa, S., Patel, R.R., Gu, M., Novaes, J., et al. (2020). Role of mitochondria in cancer immune evasion and potential therapeutic approaches. Front. Immunol. 11, 573326. https://doi.org/10.3389/fimmu.2020.573326.

110. Lee, E.G., Boone, D.L., Chai, S., Libby, S.L., Chien, M., Lodolce, J.P., and Ma, A. (2000). Failure to regulate TNF-induced NF-kappaB and cell death responses in A20-deficient mice. Science 289, 2350–2354. https://doi.org/10.1126/science.289.5488.2350.

111. Jin, Z., Li, Y., Pitti, R., Lawrence, D., Pham, V.C., Lill, J.R., and Ashkenazi, A. (2009). Cullin3-based polyubiquitination and p62-dependent aggregation of caspase-8 mediate extrinsic apoptosis signaling. Cell 137, 721–735. https://doi.org/10.1016/j.cell.2009.03.015.

112. Onizawa, M., Oshima, S., Schulze-Topphoff, U., Oses-Prieto, J.A., Lu, T., Tavares, R., Prodhomme, T., Duong, B., Whang, M.I., Advincula, R., et al. (2015). The ubiquitin-modifying enzyme A20 restricts ubiquitination of the kinase RIPK3 and protects cells from necroptosis. Nat. Immunol. 16, 618–627. https://doi.org/10.1038/ni.3172.

113. Chu, Y., Vahl, J.C., Kumar, D., Heger, K., Bertossi, A., Wójtowicz, E., Soberon, V., Schenten, D., Mack, B., Reutelshöfer, M., et al. (2011). B cells lacking the tumor suppressor TNFAIP3/A20 display impaired differentiation and hyperactivation and cause inflammation and autoimmunity in aged mice. Blood 117, 2227–2236. https://doi.org/10.1182/blood-2010-09-306019.

114. Hammer, G.E., Turer, E.E., Taylor, K.E., Fang, C.J., Advincula, R., Oshima, S., Barrera, J., Huang, E.J., Hou, B., Malynn, B.A., et al. (2011). Expression of A20 by dendritic cells preserves immune homeostasis and prevents colitis and spondyloarthritis. Nat. Immunol. 12, 1184–1193. https://doi.org/10.1038/ni.2135.

115. Duong, B.H., Onizawa, M., Oses-Prieto, J.A., Advincula, R., Burlingame, A., Malynn, B.A., and Ma, A. (2015). A20 restricts ubiquitination of pro-interleukin-1beta protein complexes and suppresses NLRP3 inflammasome activity. Immunity 42, 55–67. https://doi.org/10.1016/j.immuni.2014.12.031.

116. Setten, R.L., Rossi, J.J., and Han, S.P. (2019). The current state and future directions of RNAi-based therapeutics. Nat. Rev. Drug Discov. 18, 421–446. https://doi.org/10.1038/s41573-019-0017-4.

117. Békés, M., Langley, D.R., and Crews, C.M. (2022). Protac targeted protein degraders: the past is prologue. Nat. Rev. Drug Discov. 21, 181–200. https://doi.org/10.1038/s41573-021-00371-6.

118. Sharma, J., and Larkin, J., 3rd (2019). Therapeutic implication of SOCS1 modulation in the treatment of autoimmunity and cancer. Front. Pharmacol. 10, 324. https://doi.org/10.3389/fphar.2019.00324.

119. Ilangumaran, S., Bobbala, D., and Ramanathan, S. (2017). SOCS1: regulator of T cells in autoimmunity and cancer. Curr. Top. Microbiol. Immunol. 410, 159–189. https://doi.org/10.1007/82_2017_63.

120. Thaventhiran, J.E.D., Lango Allen, H., Burren, O.S., Rae, W., Greene, D., Staples, E., Zhang, Z., Farmery, J.H.R., Simeoni, I., Rivers, E., et al. (2020). Whole-genome sequencing of a sporadic primary immunodeficiency cohort. Nature 583, 90–95. https://doi.org/10.1038/s41586-020-2265-1.

121. Svensson, M.N., Doody, K.M., Schmiedel, B.J., Bhattacharyya, S., Panwar, B., Wiede, F., Yang, S., Santelli, E., Wu, D.J., Sacchetti, C., et al. (2019). Reduced expression of phosphatase PTPN2 promotes pathogenic conversion of Tregs in autoimmunity. J. Clin. Invest. 129, 1193–1210. https://doi.org/10.1172/JCI123267.

122. Johnson, W.E., Li, C., and Rabinovic, A. (2007). Adjusting batch effects in microarray expression data using empirical Bayes methods. Biostatistics 8, 118–127. https://doi.org/10.1093/biostatistics/kxj037.

123. Zeng, Z., Wong, C.J., Yang, L., Ouardaoui, N., Li, D., Zhang, W., Gu, S., Zhang, Y., Liu, Y., Wang, X., et al. (2022). TISMO: syngeneic mouse tumor database to model tumor immunity and immunotherapy response. Nucleic Acids Res. 50, D1391–D1397.

124. Stuart, T., Butler, A., Hoffman, P., Hafemeister, C., Papalexi, E., Mauck, W.M., 3rd, Hao, Y., Stoeckius, M., Smibert, P., and Satija, R. (2019). Comprehensive integration of single-cell data. Cell 177, 1888–1902.e21. https://doi.org/10.1016/j.cell.2019.05.031.

125. Dobin, A., Davis, C.A., Schlesinger, F., Drenkow, J., Zaleski, C., Jha, S., Batut, P., Chaisson, M., and Gingeras, T.R. (2013). STAR: ultrafast universal RNA-seq aligner. Bioinformatics 29, 15–21. https://doi.org/10.1093/bioinformatics/bts635.

126. Love, M.I., Huber, W., and Anders, S. (2014). Moderated estimation of fold change and dispersion for RNA-seq data with DESeq2. Genome Biol. 15, 550. https://doi.org/10.1186/s13059-014-0550-8.

127. Li, W., Xu, H., Xiao, T., Cong, L., Love, M.I., Zhang, F., Irizarry, R.A., Liu, J.S., Brown, M., and Liu, X.S. (2014). MAGeCK enables robust identification of essential genes from genome-scale CRISPR/Cas9 knockout screens. Genome Biol. 15, 554. https://doi.org/10.1186/s13059-014-0554-4.

128. Yang, L., Wang, J., Altreuter, J., Jhaveri, A., Wong, C.J., Song, L., Fu, J., Taing, L., Bodapati, S., Sahu, A., et al. (2023). Tutorial: integrative computational analysis of bulk RNA-sequencing data to characterize tumor immunity using RIMA. Nat. Protoc. 18, 2404–2414. https://doi.org/10.1038/s41596-023-00841-8.

129. Patro, R., Duggal, G., Love, M.I., Irizarry, R.A., and Kingsford, C. (2017). Salmon provides fast and bias-aware quantification of transcript expression. Nat. Methods 14, 417–419. https://doi.org/10.1038/nmeth.4197.

130. Barrett, T., Wilhite, S.E., Ledoux, P., Evangelista, C., Kim, I.F., Tomashevsky, M., Marshall, K.A., Phillippy, K.H., Sherman, P.M., Holko, M., et al. (2013). NCBI GEO: archive for functional genomics data sets–update. Nucleic Acids Res. 41, D991–D995. https://doi.org/10.1093/nar/gks1193.

131. Athar, A., Füllgrabe, A., George, N., Iqbal, H., Huerta, L., Ali, A., Snow, C., Fonseca, N.A., Petryszak, R., Papatheodorou, I., et al. (2019). ArrayExpress update - from bulk to single-cell expression data. Nucleic Acids Res. 47, D711–D715. https://doi.org/10.1093/nar/gky964.

132. Haghverdi, L., Lun, A.T.L., Morgan, M.D., and Marioni, J.C. (2018). Batch effects in single-cell RNA-sequencing data are corrected by matching mutual nearest neighbors. Nat. Biotechnol. 36, 421–427. https://doi.org/10.1038/nbt.4091.

133. Becht, E., McInnes, L., Healy, J., Dutertre, C.A., Kwok, I.W.H., Ng, L.G., Ginhoux, F., and Newell, E.W. (2018). Dimensionality reduction for visualizing single-cell data using UMAP. Nat. Biotechnol. https://doi.org/10.1038/nbt.4314.

134. Traag, V.A., Waltman, L., and van Eck, N.J. (2019). From Louvain to Leiden: guaranteeing well-connected communities. Sci. Rep. 9, 5233. https://doi.org/10.1038/s41598-019-41695-z.

135. Xu, C., and Su, Z. (2015). Identification of cell types from single-cell transcriptomes using a novel clustering method. Bioinformatics 31, 1974–1980. https://doi.org/10.1093/bioinformatics/btv088.

136. Wang, C., Sun, D., Huang, X., Wan, C., Li, Z., Han, Y., Qin, Q., Fan, J., Qiu, X., Xie, Y., et al. (2020). Integrative analyses of single-cell transcriptome and regulome using Maestro. Genome Biol. 21, 198. https://doi.org/10.1186/s13059-020-02116-x.

137. Sun, D., Wang, J., Han, Y., Dong, X., Ge, J., Zheng, R., Shi, X., Wang, B., Li, Z., Ren, P., et al. (2021). TISCH: a comprehensive web resource enabling interactive single-cell transcriptome visualization of tumor microenvironment. Nucleic Acids Res. 49, D1420–D1430. https://doi.org/10.1093/nar/gkaa1020.

138. Müller, C., Schillert, A., Röthemeier, C., Trégouët, D.A., Proust, C., Binder, H., Pfeiffer, N., Beutel, M., Lackner, K.J., Schnabel, R.B., et al. (2016). Removing batch effects from longitudinal gene expression - quantile normalization plus ComBat as best approach for microarray transcriptome data. PLoS One 11, e0156594. https://doi.org/10.1371/journal.pone.0156594.

139. Aran, D., Hu, Z., and Butte, A.J. (2017). xCell: digitally portraying the tissue cellular heterogeneity landscape. Genome Biol. 18, 220. https://doi.org/10.1186/s13059-017-1349-1.

140. Finotello, F., Mayer, C., Plattner, C., Laschober, G., Rieder, D., Hackl, H., Krogsdam, A., Loncova, Z., Posch, W., Wilflingseder, D., et al. (2019). Molecular and pharmacological modulators of the tumor immune contexture revealed by deconvolution of RNA-seq data. Genome Med. *11*, 34. https://doi.org/10.1186/s13073-019-0638-6.

141. Newman, A.M., Liu, C.L., Green, M.R., Gentles, A.J., Feng, W., Xu, Y., Hoang, C.D., Diehn, M., and Alizadeh, A.A. (2015). Robust enumeration of cell subsets from tissue expression profiles. Nat. Methods *12*, 453–457. https://doi.org/10.1038/nmeth.3337.

142. Li, T., Fan, J., Wang, B., Traugh, N., Chen, Q., Liu, J.S., Li, B., and Liu, X.S. (2017). TIMER: A web server for comprehensive analysis of tumor-infiltrating immune cells. Cancer Res. *77*, e108–e110. https://doi.org/10.1158/0008-5472.CAN-17-0307.

143. Wolf, F.A., Angerer, P., and Theis, F.J. (2018). SCANPY: large-scale single-cell gene expression data analysis. Genome Biol. *19*, 15. https://doi.org/10.1186/s13059-017-1382-0.

144. Zhou, Y., Zhou, B., Pache, L., Chang, M., Khodabakhshi, A.H., Tanaseichuk, O., Benner, C., and Chanda, S.K. (2019). Metascape provides a biologist-oriented resource for the analysis of systems-level datasets. Nat. Commun. *10*, 1523. https://doi.org/10.1038/s41467-019-09234-6.

145. Subramanian, A., Tamayo, P., Mootha, V.K., Mukherjee, S., Ebert, B.L., Gillette, M.A., Paulovich, A., Pomeroy, S.L., Golub, T.R., Lander, E.S., et al. (2005). Gene set enrichment analysis: a knowledge-based approach for interpreting genome-wide expression profiles. Proc. Natl. Acad. Sci. USA *102*, 15545–15550. https://doi.org/10.1073/pnas.0506580102.

146. Wu, T., Hu, E., Xu, S., Chen, M., Guo, P., Dai, Z., Feng, T., Zhou, L., Tang, W., Zhan, L., et al. (2021). clusterProfiler 4.0: A universal enrichment tool for interpreting omics data. Innovation (Camb.) *2*, 100141. https://doi.org/10.1016/j.xinn.2021.100141.

147. Liberzon, A., Birger, C., Thorvaldsdóttir, H., Ghandi, M., Mesirov, J.P., and Tamayo, P. (2015). The Molecular Signatures Database (MSigDB) hallmark gene set collection. Cell Syst. *1*, 417–425. https://doi.org/10.1016/j.cels.2015.12.004.

148. Szklarczyk, D., Kirsch, R., Koutrouli, M., Nastou, K., Mehryary, F., Hachilif, R., Gable, A.L., Fang, T., Doncheva, N.T., Pyysalo, S., et al. (2023). The STRING database in 2023: protein-protein association networks and functional enrichment analyses for any sequenced genome of interest. Nucleic Acids Res. *51*, D638–D646. https://doi.org/10.1093/nar/gkac1000.

STAR★METHODS

KEY RESOURCES TABLE

REAGENT or RESOURCE	SOURCE	IDENTIFIER
Antibodies		
A20/TNFAIP3 (D13H3) Rabbit Monoclonal Antibody	Cell Signaling Technology	Cat# 5630; RRID: AB_10698880
ABIN-1 antibody	Cell Signaling Technology	Cat# 4664; RRID: AB_10547137
Anti-TNFAIP3 antibody	Abcam	Cat# ab92324; RRID: AB_10561788
APC anti-human CD45 antibody	BioLegend	Cat# 304012; RRID: AB_314400
APC anti-mouse-CD4	BioLegend	Cat# 100412; RRID: AB_312697
anti-mouse PD-1 (CD279)	Bio X Cell	Cat# BE0273; RRID: AB_2687796
APC anti-mouse CD45 antibody	BioLegend	Cat# 103112; RRID: AB_312977
APC anti-mouse IFN-γ	BioLegend	Cat# 505809; RRID: AB_315403
anti-mouse CD28	Bio X Cell	Cat# BE0015-1; RRID: AB_1107624
anti-mouse CD3ε	Bio X Cell	Cat# BE0001-1; RRID: AB_1107634
anti-human CD3	BioLegend	Cat# 317326; RRID: AB_11150592
anti-human CD28	BD Biosciences	Cat# 555725; RRID: AB_396068
β-Actin (13E5) Rabbit mAb	Cell Signaling Technology	Cat# 4970; RRID: AB_2223172
Brilliant Violet 421™ anti-mouse CD45 Antibody	BioLegend	Cat# 103133; RRID: AB_10899570
Caspase-8 (D35G2) Rabbit mAb	Cell Signaling Technology	Cat# 4790; RRID: AB_10545768
FADD Antibody (G-4)	Santa Cruz Biotechnology	Cat# sc-271748; RRID: AB_10708849
FITC anti-mouse-CD3	BioLegend	Cat# 100204; RRID: AB_312661
Goat anti-Rabbit IgG (H+L) Cross-Adsorbed Secondary Antibody	Invitrogen	Cat# A-11008; RRID: AB_143165
Goat anti-Mouse IgG (H+L) Cross-Adsorbed Secondary Antibody	Invitrogen	Cat# A-11005; RRID: AB_141372
Normal Rabbit IgG	Cell Signaling Technology	Cat# 2729; RRID: AB_1031062
PE anti-mouse-CD8a	BioLegend	Cat# 100708; RRID: AB_312747
PE/Cyanine7 anti-Granzyme B	BioLegend	Cat# 372214; RRID: AB_2728381
RIP (D94C12) XP® Rabbit mAb	Cell Signaling Technology	Cat# 3493; RRID: AB_2305314
TNFAIP3 Monoclonal antibody	Proteintech	Cat# 66695-1-Ig; RRID: AB_2882048
TruStain FcX™ (anti-mouse CD16/32) Antibody	BioLegend	Cat# 101320; RRID: AB_1574975
Bacterial and virus strains		
Stbl3 Competent Cell	AlpaLife	Cat# KTSM110
Chemicals, peptides, and recombinant proteins		
2-mercaptoethanol	Gibco	Cat# 21985023
Antifade Mounting Medium	Beyotime	Cat# P0126
BbsI-HF®	NEB	Cat# R3539L
BIOLOGIX 70 μm Cell Strainer	BIOLOGIX	Cat# 15-1070
Brefeldin A Solution (1,000X)	BioLegend	Cat# 420601
BSA	Amresco	Cat# 0332
CellTrace CFSE Cell Proliferation Kit, for flow cytometry	Invitrogen	Cat# C34554
CellTrace Violet Cell Proliferation Kit, for flow cytometry	Invitrogen	Cat# C34557
Collagenase Type IV	Sigma-Aldrich	Cat# C5138
DAPI	Cell Signaling Technology	Cat# 4083S
DAPI	Thermo Scientific	Cat# 62248
DNase Type IV	Sigma-Aldrich	Cat# D5205
Dulbecco's Modified Eagle Medium (DMEM) basic (1 X)	Gibco	Cat# C11995500BT
EasySep™ buffer	Stem Cell	Cat# 20144

(Continued on next page)

Continued

REAGENT or RESOURCE	SOURCE	IDENTIFIER
FastDigest Esp3I	Thermo Scientific	Cat# FD0454
Fetal Bovine Serum (FBS)	Gibco	Cat# 10091148
Fetal Bovine Serum (FBS)	Biological Industries	Cat# 04-001-1ACS
gentleMACS™ C Tubes	Miltenyi Biotec	Cat# 130-093-237
Glass coverslips	NEST	Cat# 801010
GlutaMAX™	Gibco	Cat# 10564011
HEPES (1M)	Gibco	Cat# 15630080
Hexadimethrine bromide polybrene	MCE	Cat# HY-112735
Hyaluronidase Type V	Sigma-Aldrich	Cat# H6254
Intracellular Fixation & Permeabilization Buffer	Invitrogen	Cat# 88-8824-00
L-Glutamine (200 mM)	Gibco	Cat# 25030-081
Mojosort™ Buffer	Biolegend	Cat# 480017
M5 HiPer ECL Western HRP Substrate	Mei5 Biotechnology	Cat# MF074-01
Non-Essential Amino Acids, NEAA	Gibco	Cat# 11140050
Opti-MEM	Gibco	Cat# 31985070
Permeabilization buffer	Invitrogen	Cat# 00-8333-56
Penicillin-Streptomycin	Thermo Scientific	Cat# 15140122
Phosphate-Buffered Saline (PBS), pH 7.4 basic (1X)	Gibco	Cat# 10010500BT
Protease inhibitors	Sigma Aldrich	Cat# 11873580001
Protein G beads	Cytiva	Cat# 17061801
Puromycin	Invitrogen	Cat# ant-pr-1
Recombinant Human IL-2	R&D Systems	Cat# 202-IL-500
Recombinant Mouse IL-2	BioLegend	Cat# 575406
Recombinant Murine TNFa	PeproTech	Cat# 315-01A
Roswell Park Memorial Institute (RPMI) 1640 basic (1X)	Gibco	Cat# 11875500BT
Sodium Pyruvate (100 mM)	Gibco	Cat# 11360070
SIINFEKL/ OVA Peptide (257-264)	GenScript	Cat# RP10611
T4 Polynucleotide Kinase	NEB	Cat# M0201S
Trypsin-EDTA (0.05%), phenol red	Gibco	Cat# 25200-072
WB/IP lysis buffer	Beyotime	Cat# P0013
Critical commercial assays		
Bca Protein Assay Kit	Solarbio® LIFE SCIENCES	Cat# PC0020
EasySep™ Human CD8+ T Cell Isolation Kit	Stem Cell	Cat# 17953
MojoSort™ Mouse CD8+ T Cell Isolation Kit	BioLegend	Cat# 480007
NucleoSpin Gel and PCR Clean-up	MACHEREY-NAGEL	Cat# 740609.250
NucleoSpin Plasmid Transfection-grade	MACHEREY-NAGEL	Cat# 740490.250
PE Annexin V Apoptosis Detection Kit	BD Biosciences	Cat# 559763
RNAsimple Total RNA kit	TIANGEN	Cat# DP419
RNA-seq Library Prep Kit for Illumina®	Vazyme	Cat# NR604-01/02
Zombie-NIR Fixable Viability Kit	BioLegend	Cat# 423106
Deposited data		
Raw and analyzed data	This paper	GEO: GSE261915
CRC spatial transcriptomics dataset	10x Genomics	https://www.10xgenomics.com/datasets/human-colorectal-cancer-whole-transcriptome-analysis-1-standard-1-2-0
BRCA spatial transcriptomics dataset	10x Genomics	https://www.10xgenomics.com/resources/datasets/human-breast-cancer-ductal-carcinoma-in-situ-invasive-carcinoma-ffpe-1-standard-1-3-0
Pan-cancer tumor-infiltrating CD8+ T cells scRNA-Seq data	Zheng et al.[95]	GEO: GSE156728

(Continued on next page)

Continued

REAGENT or RESOURCE	SOURCE	IDENTIFIER
Experimental models: Cell lines		
Mouse: B16F10	Deng Pan Lab, Tsinghua University, Beijing	RRID: CVCL_0159
Mouse: LLC	Deng Pan Lab, Tsinghua University, Beijing	RRID: CVCL_4358
Mouse: MC38	Deng Pan Lab, Tsinghua University, Beijing	RRID: CVCL_B288
Human: SW480	Deng Pan Lab, Tsinghua University, Beijing	RRID: CVCL_0546
Human: SW620	Meisen Chinese Tissue Culture Collections, Zhejiang	Cat# CTCC-001-0353; RRID: CVCL_0547
Human: A549	Deng Pan Lab, Tsinghua University, Beijing	RRID:CVCL_0023
Human: PANC1	Deng Pan Lab, Tsinghua University, Beijing	RRID:CVCL_0480
Human: SNU398	Meisen Chinese Tissue Culture Collections, Zhejiang	Cat# CTCC-400-0145; RRID: CVCL_0077
Human: HEK293T	Deng Pan Lab, Tsinghua University, Beijing	RRID: CVCL_0063
Experimental models: Organisms/strains		
Mouse: C57BL/6-Tg(TcraTcrb)1100Mjb/J or OT-I	The Jackson Laboratory	RRID: IMSR_JAX:003831
Mouse: C57BL/6J	Peking University	RRID: IMSR_JAX:000664
Recombinant DNA		
LentiCRISPRv2-Puro	Addgene	RRID: Addgene_52961
psPAX2	Addgene	RRID: Addgene_12260
pMD2.G	Addgene	RRID: Addgene_12259
pHAGE-EF1aL-eGFP-W	Addgene	RRID: Addgene_126686
Software and algorithms		
GraphPad Prism 9	GraphPad	RRID: SCR_002798
FlowJo 10	BD Biosciences	RRID: SCR_008520
Seurat v3.1.2	Stuart et al.[124]	RRID: SCR_007322
STAR v2.6.1d	Dobin et al.[125]	RRID: SCR_004463
DESeq2 v1.34.0	Love et al.[126]	RRID: SCR_000154
MAGeCK	Li et al.[127]	https://sourceforge.net/p/mageck/ wiki/Home/
RNA-Seq immune analysis pipeline (RIMA)	Yang et al.[128]	https://github.com/liulab-dfci/RIMA
Salmon v0.13.1	Patro et al.[129]	http://samtools.sourceforge.net/
Other		
ICRAFT website	This paper	https://icraft.pku-genomics.org/
The Python code for the crawler and parser developed for ICRAFT	This paper	https://github.com/zenglab-pku/ICRAFT_A20_paper

EXPERIMENTAL MODEL AND STUDY PARTICIPANT DETAILS

Animal studies

All experiments were conducted using specific-pathogen-free (SPF) mice aged 6~8 weeks. OT-1-Cas9 mice were a kind gift from Pan lab. WT C57BL/6 mice were purchased from the Department of Experimental Animal Science, Peking University Health Science Center, Beijing, China. All mice were housed and treated in compliance with the AAIS-ZengZX-1 protocol, approved by the Association for Assessment and Accreditation of Laboratory Animal Care International and the Institutional Animal Care and Use Committee (IACUC) of Peking University. Mice were housed in facilities free of pathogens.

Cell lines

The B16F10, MC38, LLC, A549, PANC1, and HEK293T cell lines, were kind gifts from Pan lab (Deng Pan, Tsinghua University), which were cultured in DMEM (Gibco, Cat# C11995500BT). SW480 cells were also from Pan lab, which were cultured in RPMI 1640 medium (Gibco, Cat# C11875500BT). SW620 (Cat# CTCC-001-0353) and SNU398 (Cat# CTCC-400-0145) cells, purchased from MeisenCTCC, were cultured in DMEM. Both DMEM and RPMI 1640 were supplemented with 10% fetal bovine serum (FBS, Biological Industries, Cat# 04-001-1ACS), 100 µg/mL penicillin, and 100 U/mL streptomycin (1% Pen-Strep, Thermo, Cat# 15140122). All the cell lines were incubated at 37 °C with 5% CO_2.

METHOD DETAILS

Generation of genetically ablated cancer cell lines and T cells

To generate sg*TNFAIP3*, sg*TNIP1*, and sgCtrl cancer cell lines, sgRNAs targeting *TNFAIP3*, *TNIP1*, or a non-coding intergenic sequence were cloned into the LentiCRISPR v2 vector (RRID: Addgene_52961) and verified through Sanger sequencing. Lentiviruses were produced by co-transfecting 9 µg sgRNA constructs with 6 µg psPAX2 (RRID: Addgene_12260) and 3 µg pMD2.G (RRID: Addgene_12259) using 54 µL PEI in Opti-MEM (Gibco, Cat# 31985070) for each 10-cm dish. Viruses were harvested 48 hours after transfection and utilized to transduce B16F10, MC38, LLC, SW620, SW480, A549, PANC1, and SNU398 cells. Puromycin selection was applied to establish the genetically ablated cell lines. The LLC-OVA cell lines were engineered to stably express full-length OVA by lentiviral infection. SW620, SW480, PANC1, and SNU398 cells, all of which express the endogenous HLA-A2 allele, were infected with lentivirus encoding NY-ESO-1 antigen linked with eGFP (RRID: Addgene_126686). For the construction of A549-NY-ESO-1 cells, the lentiviral construct encoded the HLA-A*02:01 heavy chain, which is required for presenting the NY-ESO-1 antigen to the NY-ESO-1-specific TCR used in this study.

For T cell editing, sgRNAs targeting *Tnfaip3* or a non-coding intergenic sequence were inserted into the PMY-sgRNA-GFP vector and verified through Sanger sequencing. Retroviruses were produced by co-transfecting 9 µg sgRNA constructs with 9 µg packaging plasmids using 54 µL PEI in Opti-MEM for each 10-cm dish. Viruses were harvested 48 hours after transfection. OT-1 T cells were activated as described below and then underwent retroviral transduction through spin infection to introduce the sgRNAs. The GFP+ cells were sorted by FACS, and the genetic deletion efficiency was verified by western blot.

The sgRNA sequences were as follows:

sgCtrl in murine cells: AGAGATGAGACAAACTACCC.

sgCtrl in human cells: CATATAAGTGCTTACCAATG.

sg*Tnfaip3*-1 in murine cancer cells: GCAGCTTGTCAGTACATGTG.

sg*Tnfaip3*-2 in murine cancer cells: ATATCCATGAGTGATAGCTG.

sg*TNFAIP3*-1 in human cancer cells: CCACTTGTTAACAGAGACCG.

sg*TNFAIP3*-2 in human cancer cells: TATGCCATGAGTGCTCAGAG.

sg*Tnfaip3*-1 in murine T cells: GCCCCGAGGAAACCGCTGG.

sg*Tnfaip3*-2 in murine T cells: GCAGCTTGTCAGTACATGTG.

sg*TNIP1*-1 in human cancer cells: CAAGTCCAAGATTGAAATGG.

sg*TNIP1*-2 in human cancer cells: ATCAGGTTGCCGTCCTCACG.

sg*Tnfrsf1a* in murine cancer cells: AGTTGCAAGACATGTCGGAA.

CD8⁺ T cell activation and proliferation experiments

Primary OT-1-Cas9 cells were extracted from the spleens and lymph nodes of OT-1-Cas9 mice using MojoSort™ Mouse CD8⁺ T Cell Isolation Kit (BioLegend, Cat# 480007) according to the manufacturer's protocol. Cells were seeded in a 6-well plate and activated for 24 hours using anti-mouse CD28 (Bio X Cell, Cat# BE0015-1, RRID: AB_1107624) and anti-mouse CD3 (Bio X Cell, Cat# BE0001-1, RRID: AB_1107634) antibodies. Activated mouse OT-1-Cas9 cells were transduced with sgRNAs using retrovirus by spin infection and cultured in mouse T cell medium (RPMI 1640 with 10% FBS, 20 mM HEPES, 1 mM sodium pyruvate, 0.05 mM 2-mercaptoethanol, 2 mM L-glutamine, 100 U/mL streptomycin, and 100 µg/mL penicillin), supplemented with 20 ng/mL recombinant mouse IL-2 (BioLegend, Cat# 575406) for 7 days before co-culturing with cancer cells. Primary human CD8⁺ T cells were isolated from peripheral blood mononuclear cells with EasySep™ Human CD8⁺ T Cell Isolation Kit (Stem Cell, Cat# 17953) and activated using anti-human CD3 (BioLegend, Cat# 317326) and anti-human CD28 (BD Biosciences, Cat# 555725) antibodies in the presence of fibronectin. Activated human CD8⁺ T cells underwent lentiviral transduction via spin infection to introduce NY-ESO-1-specific TCR. Then the cells underwent expansion in human T cell medium (RPMI 1640 with 10% FBS, 1 mM sodium pyruvate, 2 mM L-glutamine, 2 mM GlutaMAX, 100 U/mL streptomycin, and 100 µg/mL penicillin) supplemented with 10 ng/mL recombinant human IL-2 (R&D Systems, Cat# 202-IL-500).

sg*TNFAIP3* A549 or OT-1 cells bulk RNA-Seq samples preparation

SgCtrl or sg*TNFAIP3* A549 cells were subjected to total RNA extraction using RNAsimple Total RNA kit (TIANGEN, Cat# DP419) according to the manufacturer's instructions. To compare transcriptional profiles of sgCtrl and sg*Tnfaip3* CD8⁺ T cells, we co-cultured sgCtrl or sg*Tnfaip3* CD8⁺ T cells with OVA peptide (257-264 aa, SIINFEKL)-pulsed LLC cells for 4 hours. Then the CD8⁺ T cells were sorted by FACS, and total RNA was extracted following the manufacturer's protocol. RNA samples from each experiment were sent

to Annoroad Gene Technology for sequencing. Using 1~3 μg of RNA, RNA-Seq libraries were prepared using VAHTS Universal V6 RNA-Seq Library Prep Kit for Illumina® (NR604-01/02) following manufacturer's guidelines.

CD8+ T cell cytokine production experiments

Naive OT-1 T cells were isolated from the spleens of OT-1 transgenic mice using the MojoSort Mouse CD8+ T Cell Isolation kit, followed by activation and expansion as previously described. For cytokine production assay, both *Tnfaip3*-null and control-edited OT-1 T cells were incubated with 100 ng/mL OVA peptide (257-264 aa, SIINFEKL) for 4 hours in the presence of 5 μg/mL Brefeldin A (BFA; BioLegend, Cat# 420601) at day 7~12 post-activation. The cells were collected for intracellular staining. Firstly, they were stained with Zombie-NIR Fixable Viability Kit (BioLegend, Cat# 423106) in PBS for 5 min and then stained with PE anti-mouse CD8 antibody (BioLegend, Cat# 100707) in FACS buffer (PBS + 5% FBS) at room temperature (RT) for 15 minutes. Before intracellular cytokine staining, the cells were fixed and permeabilized using Intracellular Fixation & Permeabilization Buffer Set (Invitrogen, Cat# 88-8824-00). Then they were stained with APC anti-mouse IFN-γ (BioLegend, Cat# 505809) in permeabilization buffer (Invitrogen, Cat# 00-8333-56) at RT for 15 minutes and analyzed using flow cytometry.

CD8+ T cell target killing experiments

For the *in vitro* competitive assay in murine cell lines, the sgCtrl murine cancer cells were labeled with CFSE (BD Bioscience, Cat# 565082), mixed with sg*Tnfaip3* cells before being seeded in 12-well plates. After the cell attached, they were pulsed with OVA peptide (257-264 aa, SIINFEKL) for 2~4 hours. The cells were then co-cultured with either sgCtrl or sg*Tnfaip3* OT-1 T cells at indicated E:T (effector to target) ratio. In human cells, sgCtrl SW620-NY-ESO-1, SW480-NY-ESO-1, A549-NY-ESO-1, PANC1-NY-ESO-1, and SNU398-NY-ESO-1 cells were labeled withCTV (Invitrogen, Cat# C34557), mixed with their corresponding sg*TNFAIP3* cells and co-cultured with NY-ESO-1-specific TCR-T cells at indicated E:T ratio. 24~48 hours later, cancer cells were harvested and analyzed via flow cytometry, T cells were distinguished using APC anti-mouse CD45 antibody (BioLegend, Cat# 103112) or APC anti-human CD45 antibody (BioLegend, Cat# 304012). Dead cells were identified with DAPI (Cell Signaling Technology, Cat# 4083S) or Zombie Stain (BioLegend, Cat# 423106).

Cell apoptosis staining assay

0.5×10^6 cancer cells were seeded in each well of a 12-well plate and treated with TNF for 24 hours. After treatment, cells were harvested and stained with PE Annexin V Apoptosis Detection Kit (BD Pharmingen™, Cat# 559763) following the manufacturer's instructions and analyzed via flow cytometry.

Mouse tumor inoculation experiments

Mouse tumor models were established by subcutaneously injecting 1×10^6 LLC or 1×10^6 MC38 cells, resuspended in 100 μL PBS, into C57BL/6 mice. For anti-PD-1 treatment, 200 μg anti-PD-1 antibody (Bio X Cell, Cat# BE0273, RRID: AB_2687796) or isotype control antibody were intraperitoneally injected into mice on day 9 post tumor inoculation, then every 3 days for LLC tumors (3 times, until day 15). For OT-1 T cell adoptive transfer assay, 3×10^6 sgCtrl or sg*Tnfaip3* T cells were resuspended in 100 μL PBS, then adoptively transferred into C57BL/6 mice bearing LLC-OVA tumor on day 9. The LLC-OVA tumors were established using a LLC cell line stably expressing full-length OVA antigen via lentiviral transduction. The control group of mice that did not receive T cell transfer was injected with 100 μL PBS. Tumor sizes were measured every 3~4 days once palpable, using (length × width²)/2 for volume calculation. Endpoints were set when the tumor's longest diameter reached 2.0 cm or upon death of mouse. Age- and sex-matched mice were randomized when possible. Investigators were blinded to sample allocation during tumor size measurement when feasible.

Tumor-infiltrating lymphocyte analysis

Tumor tissues were excised and digested with Collagenase Type IV (Sigma-Aldrich, Cat# C5138), DNAse Type IV (Sigma-Aldrich, Cat# D5205) and Hyaluronidase Type V (Sigma-Aldrich, Cat# H6254) in 5 mL RPMI1640 in gentleMACS™ C Tubes (Miltenyi Biotec, Cat# 130-093-237) and incubated at 37 °C for 30 minutes then processed via GentleMACS. Single-cell suspension was obtained by filtering the digested tissue through a 70 μm cell strainer. We used Zombie-NIR Fixable Viability Kit (BioLegend, Cat# 423106) to stain cells in PBS, then stained cells with anti-mouse CD16/32 (BioLegend, Cat# 101320, RRID: AB_1574975) to block the IgG Fc receptors. Then, cells were stained with surface markers and then underwent fixation and permeabilization for intracellular staining. The used antibodies are as follows: Brilliant Violet 421™ anti-mouse-CD45 (BioLegend, Cat# 103133), FITC anti-mouse-CD3 (BioLegend, Cat# 100204), PE anti-mouse-CD8a (BioLegend, Cat# 100708), APC anti-mouse-CD4 (BioLegend, Cat# 100412), and PE/Cyanine7 anti-Granzyme B (BioLegend, Cat# 372214). Cells were analyzed by Beckman CytoFLEX S.

Western blot analysis

Cells were harvested and lysed in lysis buffer (Beyotime, Cat# P0013). Protein concentrations were determined using Bca Protein Assay Kit (Solarbio® LIFE SCIENCES, Cat# PC0020). 20 μg total protein was loaded onto SDS-PAGE and transferred to PVDF membranes. Membranes were blocked in 5% skim milk for 1 hour at RT and were incubated with indicated primary antibodies at 4 °C overnight, following incubation with secondary antibodies at RT for 1 hour. Blots were incubated in M5 HiPer ECL Western HRP Substrate (Mei5 Biotechnology, Cat# MF074-01) and captured using a ChemiDoc™ Imaging System (Bio-Rad Laboratories). The following antibodies were used: A20/TNFAIP3 mAb (Cell Signaling Technology, Cat# 5630; Abcam, Cat# ab92324), β-Actin Rabbit

mAb (Cell Signaling Technology, Cat# 4970L; loading control) and ABIN-1 (TNIP1) antibody (Cell Signaling Technology, Cat# 4664).

Co-immunoprecipitation (Co-IP)

For Co-IP experiments, cells were either treated or untreated with TNF for indicated times, then harvested and lysed in lysis buffer (Beyotime, Cat# P0013). Cell lysates were precleared with 20 μL protein G beads for 1 hour at 4°C and then immunoprecipitated overnight at 4°C with 1 mg anti-Tnfaip3 or anti-RIPK1 antibodies in the presence of 20 μL protein G beads. Subsequently, the beads underwent three washes with lysis buffer, followed by boiling and western blot analysis. The following antibodies were used: anti-RIPK1 (Cell Signaling Technology, Cat# 3493), anti-FADD (Santa Cruz Biotechnology, Cat# sc-271748), anti-caspase8 (Cell Signaling Technology, Cat# 4790S), Normal Rabbit IgG (Cell Signaling Technology, Cat# 2729).

Immunofluorescence

LLC cells were grown on glass coverslips (NEST, Cat# 801010) in 12-well plates and were treated with TNF for 1 hour. Cells were then fixed for 30 minutes with 4% paraformaldehyde (Beyotime, Cat# P0099) at RT and permeabilized with 2% Triton X-100 for 10 minutes on ice and then blocked with 1% BSA for 30 minutes. Anti-Tnfaip3 (Proteintech, Cat# 66695-1-Ig) and anti-Tnip1(Cell Signaling Technology, Cat# 4664) were used for staining in 1:200 dilution for 1 hour, followed by staining with the secondary antibody (Invitrogen, Cat# A-11005; Invitrogen, Cat# A-11008) in 1:200 dilution for 1 hour and kept in dark. Then the cells were stained with 0.1 μg/mL DAPI (Thermo, Cat# 62248) for 5 minutes. The cells were sealed with Antifade Mounting Medium (Beyotime, Cat# P0126) and imaged using a Leica microscope (Leica, TCS SP8).

Statistical analysis

Statistical analyses were performed via GraphPad Prism 9 software (RRID: SCR_002798), applying unpaired Student's t-test, one-way ANOVA, or two-way ANOVA as indicated (ns: not significant, $*P<0.05$, $**P<0.01$, $***P<0.001$, $****P<0.0001$). Group sizes for *in vitro* experiments were set based on prior experience of the experimental variability. Likewise, the group sizes for *in vivo* experiments were set based on previous experience with the corresponding tumor models.

QUANTIFICATION AND STATISTICAL ANALYSIS

CRISPR screen dataset collection and preprocessing

A Python crawler and parser were developed to retrieve datasets from the Gene Expression Omnibus (GEO),[130] covering studies from 2014 to 2022. The search strategy utilized a logical combination of keywords to identify datasets. The keywords included "scale-related" terms such as "genome-wide" and "genome-scale"; "technology-related" terms such as "CRISPR knockout", "CRISPR/Cas9", and "pooled CRISPR screening"; and "immune-related" terms including "immune", "immuno-oncology", and "immunotherapy". These keywords were used to retrieve and filter the GEO datasets. Additionally, the Python parser was developed to extract relevant papers from PubMed, applying the same keyword-matching strategy to paper abstracts. After compiling a comprehensive list of immune-related CRISPR screen studies, FASTQ files were downloaded if publicly available, or requested from corresponding authors otherwise. When FASTQ files were not available, raw count or normalized count files were collected. Screen library files were also obtained. Metadata, including study design and sample information, were extracted using the parser. Manual validation was performed to determine whether datasets should be included into the database. Detailed metadata, such as perturbed cell models, phenotypes, treatment conditions, sample information, library design, and perturbation technique, were curated from the literature. This information is presented in ICRAFT upon dataset query.

All CRISPR screen datasets were processed through the standardized pipeline MAGeCK.[127] Sequence reads were trimmed and mapped to the corresponding library using MAGeCK "count" function to quantify sgRNA read counts. Technical replicates were merge into one single sample, while biological replicates were treated as separate samples but analyzed together for variance estimation. Quality control analyses were applied to both FASTQ and count files. All control sgRNAs were assigned unique IDs before downstream analysis. The MAGeCK "test" module was then used to identify gene targets with enriched or depleted targeting sgRNAs in the treatment group compared to the control. MAGeCK generated log fold change (LFC) values for both sgRNAs and genes, reflecting their relative enrichment levels across cell populations. Given the diverse origins of samples from different studies, to mitigate batch effects, comparisons between datasets were normalized using z-score normalization at the sgRNA-level. For integrative and comparative analyses of CRISPR screens, all murine gene symbols were converted into their human homolog counterparts. Genes lacking a clear human homolog were excluded from the analyses. For the genes with multiple mouse-human mapping relationships, when converting mouse genes to human homologs, we eliminated redundancy by retaining only the highest-ranked human homolog in the ranking list.

All screens in ICRAFT were classified based on cell type, distinguishing between cancer cells and immune cells, and further categorized according to study design. This resulted in five screening categories, each with specific interpretations of gene inactivation effects. Specifically, in the "Cell viability and proliferation" category, negative scores indicate that gene deletion inhibits cell proliferation, while positive scores suggest that gene deletion promotes cell proliferation. In the "Sorting by marker expression" category, negative scores indicate gene deletion decreases marker levels, while positive scores suggest that gene deletion increases marker levels. In the "Co-culture with immune cells" category, negative scores indicate that gene deletion increases the sensitivity of cancer cells to immune cell-mediated killing, while positive scores suggest gene deletion decreases the sensitivity. In the "Co-culture with other cells" category (perturbation on immune cells), negative scores indicate that gene deletion decreases immune cell activity (e.g., proliferation or cytokine production of T cells), while positive scores indicate that gene deletion increases immune cell activity. In the

"*In vivo* CRISPR screens" category, negative scores indicate that gene deletion results in negative selection, suggesting elimination *in vivo*, while positive scores suggest that gene deletion leads to positive selection, indicating enrichment *in vivo*. For presentation consistency, we have inverted the display direction for CRISPR activation screen data. For example, in a sorting screen, if overexpression of "gene A" promotes marker expression, our data will show that deletion of "gene A" reduces marker expression (i.e., the LFC values of guide RNAs are converted from positive to negative). To prevent misinterpretation of the screen type, we explicitly labeled it as the CRISPR activation perturbation type in both the plots and the metadata tables.

Human single-cell RNA-Seq collection and preprocessing

ICRAFT database contains 83 high-quality tumor microenvironment (TME) scRNA-Seq datasets across 31 cancer types (Table S2). TME scRNA-Seq datasets were collected from GEO[130] and ArrayExpress.[131] Raw count, FPKM or TPM (if available) expression matrix of each dataset was downloaded. Sample metadata, such as the patient ID, tissue origin, and the original cell-type annotation, were curated from the original studies. For datasets containing multiple cancer types, each cancer type was processed and presented separately. A standardized pipeline was applied to reduce systematic bias introduced by technical variations in sequencing platforms, library preparation methods, and downstream analytical algorithms. We used Seurat v3.1.2[124] for quality control and data preprocessing, filtering out cells with read counts below 1,000 or fewer than 500 detected genes.

After preprocessing, different normalization methods were applied depending on the sequencing platform. For unique molecular identifier (UMI)-based technologies (10x Genomics, Drop-Seq, and inDrop), global scaling normalization was used to scale UMI counts to 10,000 per cell, followed by log-transformation to address differences in sequencing depth across cells. For data generated with the Smart-Seq2 platform, log-transformation was applied directly before downstream analyses. When raw count data were available, we converted them to TPM for standardization. Batch effects were corrected using Seurat v3.1.2.[124] Initially, feature selection was performed on each dataset, followed by feature prioritization across multiple datasets. We then applied canonical correlation analysis (CCA) to identify anchors between dataset pairs without supervision. Pairwise distances between datasets were calculated and used for hierarchical clustering. To progressively correct the batch effect, mutual nearest neighbors (MNNs)[132] were computed in the CCA subspace. After batch effect correction, uniform manifold approximation and projection (UMAP)[133] was applied for dimension reduction. Clusters were identified using the Leiden[134] and Louvain[135] algorithms. Differentially expressed genes (DEGs) between clusters were identified using the Wilcoxon test.

Malignant cell clusters were determined by combining original study annotations and checking malignant cell marker expression, such as epithelial markers (*EPCAM*, *KRT8* and *KRT18*). Normal cell clusters were automatically annotated using a marker-based method in MAESTRO[136] with DEGs between clusters and marker genes from published resources,[137] for example, stromal cells (*COL1A1*, *VWF*, and *PLVAP*), myeloid cells (*CD68*, *CLEC9A*, *CD1C*, and *S100A9*), T cells (*CD3D*, *SELL*, *CCR7*, *FOXP3*, *CTLA4*, and *CD8A*), and B cells (*MZB1*, *IGHA1*, *CD19*, and *AICDA*). We retained 23 common cell types. Manual corrections were performed to all annotated cell types after completing automatic annotation. This process involved verifying marker expression, integrating these annotations with the original cell annotations, and the identification of malignant cells conducted in the previous step.

ICB clinical trial cohort RNA-Seq data collection and preprocessing

RNA-Seq data, patient survival, and immunotherapy response of 18 cancer ICB therapy clinical trial cohorts, composed of 943 tumor samples prior to treatment, were obtained from published studies (Table S3). For each RNA-Seq dataset, the transcriptomic profile was $\log_2(1+TPM)$ transformed and quantile-normalized across patients. The batch effect between clinical cohorts was further removed by applying ComBat,[123] a method demonstrated to effectively reduce batch effects in transcriptomic datasets. As also referenced in a benchmark study,[138] the combination of quantile normalization and ComBat provided robust and reliable batch correction results. Samples were stratified based on response status, and the Wilcoxon rank-sum test was applied to statistically evaluate differences in gene expression or signature score between responders and non-responders within each cohort. While batch correction addressed confounding factors, it did not affect the expression level comparisons between groups but improved the harmonization of downstream visualization across datasets.

CCLE data collection and preprocessing

We downloaded the RNA-Seq data of 1,208 cancer cell lines and proteomic data of 373 cancer cell lines from the cancer Dependency Map (DepMap) portal (https://depmap.org/portal/download/all/),[83] which contains processed gene or protein expression data with cell line metadata. In our study, transcriptomic and proteomic data were grouped by the tissue origin of each cell line. *TNFAIP3* expression across these cell lines was visualized using box plots, with the data sorted by median expression values from low to high. For correlation analysis at the gene or protein level, we calculated Pearson correlation coefficients between *TNFAIP3* and all other genes or proteins, applying false discovery rate (FDR) correction to ensure statistical accuracy. *TNFAIP3*-null signature scores were computed for each cell line and subsequently categorized into high- and low-signature groups based on the median signature level observed across all cell lines. The Gene Ontology (GO) and Kyoto Encyclopedia of Genes and Genomes (KEGG) pathway scores were calculated by averaging the expression of genes in each pathway for every cell line. The distribution of pathway scores in both the high- and low-signature groups was analyzed and visualized using split violin plots. Linear regression analysis with FDR correction was performed to assess the correlation between each pathway score and *TNFAIP3*-null signature score across all cell lines. This method provided a comprehensive understanding of the association between the *TNFAIP3*-null signature level and various pathways.

Gene-dependency levels for *TNFAIP3*, *PTPN2*, *SOCS1*, and *GAPDH* genes based on 1,095 CRISPR-Cas9 essentiality screen datasets of the public 2023 Q2 release were downloaded from the DepMap portal. A cutoff gene-dependency level < −1 was used to determine common essential. Histograms were generated with bins spanning from the minimum to the maximum gene-dependency level at intervals of 0.025. The quantity and percentage of cell lines with gene-dependency level below -1 were annotated.

TCGA cohort data processing
Transcriptome and clinical data were obtained from the TCGA Data Portal (https://portal.gdc.cancer.gov/) for all 33 cancer types. We categorized breast cancer datasets into basal, lumA, lumB and Her2+ subtypes based on PAM50. We divided HNSC data sets into the HPV+ and HPV- subtypes, as well as SKCM into the primary and metastasis subtypes. Immune cell infiltration in the TME was estimated from bulk RNA-Seq data using xCell,[139] QUANTISEQ,[140] Cibersort,[141] and TIMER[142] algorithms.

CRISPR screen datasets integration analysis
For each curated CRISPR screen dataset, MAGeCK "test" module ranks all evaluated genes by a combination of gene perturbation effect and variation among different guides.[127] To integrate results from multiple large-scale CRISPR screens, we combined the ranked gene lists into one list, which could be formulated as a list aggregation task. Robust rank aggregation (RRA),[77] a well-established method for aggregating ranked data, was applied to integrate these ranked gene lists from CRISPR screen results. For integrative analysis on cancer cells in this study, we selected screens with a library size exceeding 10,000 genes and where the top three ranked genes had MAGeCK statistics (FDR) below 0.2. For CD8+ T cell screens, we applied the same criteria for *in vitro* screens. However, for *in vivo* CD8+ T cell screens, we used a library size exceeding 1,000 genes with the same statistical threshold. Genes that lacked a clear human homolog or had multiple mappings between human and mouse were excluded from the integrative analyses.

Analysis of gene expression in spatial transcriptomics datasets
Preprocessed spatial transcriptomics data of colorectal cancer (CRC) sample is available from 10x Genomics website https://www.10xgenomics.com/datasets/human-colorectal-cancer-whole-transcriptome-analysis-1-standard-1-2-0. Preprocessed spatial transcriptomics data of breast cancer (BRCA) sample was obtained from the 10x Genomics website https://www.10xgenomics.com/resources/datasets/human-breast-cancer-ductal-carcinoma-in-situ-invasive-carcinoma-ffpe-1-standard-1-3-0. Quality control was performed according to the standard Scanpy pipeline.[143] Spots with more than 20% mitochondrial gene counts and genes presented in fewer than 10 cells were filtered. PCA and UMAP dimensionality reduction were performed. Clustering was performed with the Leiden algorithm[134] at resolution 0.5. Spatial feature expression plots were generated with the scanpy.pl.spatial function in Scanpy v1.9.3. Average expression levels of *TNIP1* and *TNFAIP3* were calculated for each cluster in both CRC and BRCA datasets, followed by Pearson correlation analysis.

Bioinformatics and statistical analysis
Over-representation enrichment analysis
Functional enrichment analysis was performed for gene lists using Metascape.[144] GO terms for the biological process, cellular component, and molecular function categories, as well as KEGG pathways, Reactome gene sets, and CORUM were enriched. Accumulative hypergeometric P-values and enrichment factors were calculated and used for filtering.
Gene Set Enrichment Analysis (GSEA)
To characterize the functions of differentially expressed or correlated genes or proteins, GSEA[145] was performed using the R package clusterProfiler[146] v4.8.1 based on the gene ranking from the LFCs or correlative coefficients derived from the differential expression analysis or correlative analysis. KEGG pathways, GO terms, and Reactome gene sets were collected from the MSigDB.[147] Key pathways showing significant upregulation or downregulation (FDR < 0.05) were identified and presented.
Protein-protein interaction (PPI) network analysis
To elucidate the interactive relationships among dual-function gene targets, a comprehensive PPI network analysis was conducted. This analysis involved mapping all dual-function gene targets onto the STRING database v12.0[148] to visualize their interaction network. The goal was to uncover potential functional interdependencies and pathways among these targets. Subsequently, functional pathway analysis was applied to the constructed PPI network. In analyzing the network, particular attention was given to sub-graphs, defined as smaller interconnected groups within the larger network. We retained sub-graphs that comprised a minimum of three nodes. One representative pathway was selected for annotating each sub-graph. This annotation was based on the most prominent or relevant biological pathway associated with the proteins in each cluster.
Transcription factor inference
Using the LISA,[84] we analyzed two sets of DEGs derived from *TNFAIP3* ablation in A549 cells, each adhering to criteria of FDR < 0.05 and baseMean > 200. The first list included 89 upregulated genes with LFCs > 0, while the second comprised 69 downregulated genes with LFCs < 0. LISA first estimates the epigenetic model that fits these input genes, utilizing a large compendium of histone mark and chromatin accessibility profiles in the Cistrome database. It then employs TF ChIP-seq data and known DNA-binding motifs to infer the driving transcription factors. This analysis resulted in inferred TFs and enriched motifs for both gene lists, providing insights into the regulatory mechanisms influenced by *TNFAIP3* inactivation. In the case of *Tnfaip3*-null OT-1 cells, the initial thresholds (FDR < 0.05 and baseMean > 200) yielded only 63 genes. To accommodate this, we adjusted our parameters to include genes with

FDR < 0.05 and LFCs > 1 for upregulation, resulting in 470 genes, and LFCs < -1 for downregulation, identifying 86 genes. This modified approach allowed for a more comprehensive analysis of the DEGs in *Tnfaip3*-null OT-1 cells. Subsequently, the identical analysis was conducted on two lists of DEGs in *Tnfaip3*-null OT-1 cells, to identify putative TFs and DNA-binding motifs.

Pan-cancer tumor-infiltrating CD8+ T cells scRNA-Seq analysis

All processed gene expression data of pan-cancer CD8+ CTLs were obtained from GSE156728. Major cluster was annotated by marker genes and kept consistent with original paper. Downstream analysis was performed using the standard Scanpy pipeline.[143]

TNFAIP3-null signature analysis

A *TNFAIP3*-null signature was established to study the clinical relevance of *TNFAIP3* deficiency using 89 upregulated genes and 69 downregulated genes in A549 cells (*TNFAIP3* deletion vs. intergenic region-targeted deletion control, FDR<0.05 and baseMean>200), with the LFCs as weights. We calculated a *TNFAIP3*-null signature score for each input expression profile to estimate the *TNFAIP3*-deficient level using a weighted sum of the signature gene expressions based on the equation $S = \sum_{i=1}^{n}(w_i \times E_i)$, where S is the signature score, E_i is the expression level of the $i th$ gene, and w_i denotes its corresponding weight. The associations of *TNFAIP3* deficiency with immune-related pathways, T cell infiltration level in tumors, and response to ICB were evaluated.

Multivariable logistic regression analysis

To address the potential confounding effect of CD8+ T cell infiltration, we constructed logistic regression models with ICB response as the outcome variable and *TNFAIP3*-null signature as the input variable, incorporating the CD8+ T cell infiltration level as a confounding variable. We standardized both the signature and CD8+ T cell infiltration levels using z-score normalization to ensure comparability. Cohort-specific effects were adjusted using dummy variables.

Survival analysis

Survival data and genotype information for 31,127 patients from 97 cancer cohorts were obtained through cBioPortal (https://www.cbioportal.org/)[97] (Table S8). A total of 46 genes associated with autoimmune diseases, as reported in previous studies[100–106] (Table S8), were analyzed. The association between the *TNFAIP3* genotype and overall survival was evaluated using Kaplan-Meier curve, with log-rank p-value and 95% confidence intervals calculated. The Cox proportional hazards regression model was used to compare overall survival between patients with alterations in autoimmune disease-related genes and those without such alterations. The model was adjusted for key prognostic factors, including age, sex, race, and cancer type. The survival curve was generated for visual representation using the R package survminer v0.4.9.

Collection of TNFAIP3 mutation profile

We analyzed the genetic alteration characteristics of the *TNFAIP3* gene using cBioPortal. The frequency and count of alterations by mutation type were calculated across all tumor types in TCGA. The mutation frequencies and locations on *TNFAIP3* were visualized by cBioPortal. Additionally, the alteration frequency distribution in the TNFAIP3 OTU domain was visualized using COSMIC-3D.[98]

TNFAIP3-null A549 or OT-1 cells bulk RNA-Seq analysis

To enable the uniform analysis of bulk RNA-Seq data, we applied the RNA-Seq immune analysis pipeline (RIMA).[128] In brief, sequencing reads were aligned to the mouse reference genome (GRCm38 or mm10) using STAR[125] v2.6.1d. Salmon[129] v0.13.1 was utilized to map transcripts to genes and generate a gene count matrix. Differentially expressed genes were identified using DESeq2[126] v1.34.0, with an adjusted P-value (FDR) threshold of <0.05 for determining significance. The replicates of RNA-Seq from each condition were considered as a covariate in DESeq2.